

1 **Novel insights into deep groundwater exploration by geophysical estimation of**
2 **hard rock permeability**

3 **Muhammad Hasan** ^{1, 2, 3,*}, **Lijun Su** ^{1, 2, 3, **}

4 ¹ *State Key Laboratory of Mountain Hazards and Engineering Resilience, Institute of Mountain*
5 *Hazards and Environment, Chinese Academy of Sciences, Chengdu 610299, China*

6 ² *China-Pakistan Joint Research Center on Earth Sciences, CAS-HEC, Islamabad, Pakistan*

7 ³ *University of Chinese Academy of Sciences, Beijing 100049, China*

8

9 *Corresponding authors:

10 Muhammad Hasan: Email: mhasan@imde.ac.cn; ORCID: [https://orcid.org/0000-0001-6804-](https://orcid.org/0000-0001-6804-7962)
11 [7962](https://orcid.org/0000-0001-6804-7962); Phone Number: +86-13051361710

12 Lijun Su: Email: sulijun1976@163.com; ORCID: <https://orcid.org/0000-0001-9972-4698>

13 Corresponding authors' postal address: State Key Laboratory of Mountain Hazards and
14 Engineering Resilience, Institute of Mountain Hazards and Environment, Chinese Academy of
15 Sciences, Chengdu 610299, China

16

17

18

19

20

21

22

23 **Abstract**

24 Deep groundwater exploration in hard rock terrains is essential in regions with the potential for
25 deep aquifers, especially where water scarcity threatens sustainable development and long-term
26 water security. However, such exploration remains a global challenge due to the geological
27 complexity and the limitations of traditional investigation methods. Accurate estimation of
28 hydraulic parameters, particularly permeability (k), is vital for effective groundwater
29 management and reliable prediction of future scenarios. Conventionally, permeability is
30 measured through borehole investigations. While widely adopted, these methods are intrusive,
31 expensive, time-consuming, and limited to point-scale measurements. Their effectiveness is
32 often restricted to areas with relatively uniform geological settings, and they are generally
33 inadequate for assessing deep groundwater systems. In contrast, geophysical methods offer a
34 non-invasive, cost-effective, and efficient alternative, enabling large-scale assessment of
35 subsurface hydrogeological conditions with minimal surface disruption. Previous geophysical
36 studies have employed empirical approaches, particularly vertical electrical sounding (VES), to
37 estimate permeability. However, these methods are confined to shallow depths, homogeneous
38 settings, and one dimensional interpretation, making them insufficient for application in highly
39 heterogeneous hard rock environments. This study introduces, for the first time, the use of
40 controlled-source audio-frequency magnetotellurics (CSAMT) to estimate two and three
41 dimensional permeability distributions at depths exceeding 1 km in complex geological settings,
42 including sedimentary, igneous, and metamorphic rocks. The results demonstrate that CSAMT
43 can effectively characterize deep subsurface variability and generate accurate, spatially
44 continuous hydrogeological models in hard rock terrains, particularly where drilling data are
45 limited or unavailable. Our approach cuts down on the need for costly borehole tests and allows

46 for a more thorough assessment of aquifer potential. This research provides a major
47 breakthrough in deep groundwater investigation and helps with better scientific planning and
48 long-term groundwater resource management in challenging hard rock areas.

49 **Keywords:** Permeability; Geophysical methods; Hydraulic parameters; Groundwater; Hard rock;
50 Hydrogeological models

51 **1 Introduction**

52 Metamorphic and igneous rocks make up the majority of Earth's crust, covering roughly one-
53 third of the planet's surface ([Amiotte Suchet et al., 2003](#)). Research on groundwater in hard rock
54 terrains primarily aims to delineate subsurface geological features, such as fault systems and
55 fracture networks, which are essential for understanding groundwater occurrence and movement
56 ([Fernando and Pacheco, 2015](#); [Hasan et al., 2021](#)). A crucial parameter in these studies is aquifer
57 potential, which refers to the ability of rock formations to store and transmit water. This
58 parameter is essential for the monitoring and evaluation of groundwater resources ([Majumdar
59 and Das, 2011](#); [Nwosu et al., 2013](#); [Qian et al., 2024](#)). The aquifer potential is influenced by
60 various geological and environmental factors, such as lithology, structural configuration, fault
61 and joint density, mineralogical composition, weathering degree, and water infiltration depth
62 ([Dell'Oca et al., 2020](#); [Abbas et al., 2022](#)). Accurately characterizing the lateral and vertical
63 heterogeneity of aquifer properties within complex and massive rock units remains one of the
64 primary challenges in hard rock hydrogeology ([Courtois et al., 2010](#); [Dewandel et al., 2006](#)). A
65 thorough assessment of aquifer potential is particularly important in geologically varied
66 environments, where conventional methods frequently prove inadequate due to the complexity of
67 subsurface formations and the scarcity of direct data ([Robinson et al., 2016](#); [Worthington et al.,](#)

68 2016; Zhu et al., 2017). These uncertainties often lead to inefficient or unsustainable
69 groundwater development, worsening water scarcity and environmental degradation (Dewandel
70 et al., 2006; Refsgaard et al., 2012; Lachassagne et al., 2021). Refining cost-effective and
71 reliable methods for assessing subsurface hydrogeological conditions is a fundamental challenge
72 in the study and management of hard rock aquifers.

73 Groundwater at depths greater than 500 m is typically less affected by surface
74 hydrological processes and frequently contains brackish or saline water (Gleeson et al., 2016;
75 Margat and van der Gun, 2013; Ferguson et al., 2023). Its exploration is increasingly recognized
76 as strategically important in certain geological and environmental contexts. In the Jinji region
77 (study area), various site-specific factors require a targeted examination of these deeper reserves.
78 First, surface water availability is both scarce and unreliable, increasing the importance of deep
79 aquifers as a potential supplementary source of freshwater. Second, the shallow subsurface is
80 largely composed of fresh granite, a rock type known for its inherently low porosity and
81 permeability, thus offering limited groundwater potential (Dewandel et al., 2006; Lachassagne et
82 al., 2021). In contrast, favorable water-bearing zones such as fractured granite, sandstone, and
83 hornstone are typically found at much greater depths. Third, recent national water initiatives in
84 China have underscored the need for deep subsurface exploration, especially in structurally
85 complex terrains, to uncover underutilized aquifers that could contribute to more resilient water
86 supply systems in the face of increasing demand and climatic uncertainties (MOHURD, 2021;
87 Qian et al., 2024). Comprehensive assessments of deep groundwater are therefore essential for
88 identifying these hidden but strategically valuable water sources, evaluating their recharge
89 characteristics, and integrating them into sustainable long-term management plans (Courtois et
90 al., 2010; Refsgaard et al., 2012). As pressures on surface and shallow subsurface water sources

Formatted: Font: (Default) Times New Roman, 12 pt

Formatted: Font: (Default) Times New Roman, 12 pt

Formatted: Font: (Default) Times New Roman, 12 pt

91 [intensify, deeper aquifer systems may serve as a critical buffer, ensuring more reliable water](#)
92 [access amid growing environmental and socio-economic challenges.](#)

93 Multiple studies have recorded the swift depletion of global groundwater reserves,
94 underscoring an increasing concern for water sustainability (Rodell et al., 2009; Wada et al.,
95 2010; Laghari et al., 2012; Jasechko et al., 2024). In light of this significant issue, thorough and
96 precise assessments of groundwater resources are crucial for their effective management and
97 sustainable utilization. A comprehensive understanding of hydraulic properties is essential for
98 these assessments. Permeability is a crucial parameter for characterizing the ability of geological
99 formations to store and transmit water. This factor is crucial for aquifer analysis in various
100 hydrogeological contexts globally (Dewandel et al., 2006; Gerke et al., 2011; Allègre et al., 2016;
101 Fiandaca et al., 2018; Mudunuru et al., 2022; Esmailpour et al., 2023; Yan et al., 2024; Carbillet
102 et al., 2024). The aquifer potential of geological layers is usually determined by permeability
103 (Zhang et al., 2004; Pellet et al., 2024). De Lima and Niwas (2000), Soupios et al. (2007), Hasan
104 et al. (2021), and Yang and Zhang (2024) all state that borehole testing is the standard method
105 for measuring aquifer parameters. While boreholes contribute valuable geological data,
106 generating a comprehensive 2D analysis through drilling alone is often time-consuming and
107 challenging (Hubbard and Rubin, 2002; Niwas and De Lima, 2003). Borehole methods are
108 limited by high costs, time-intensive procedures, bulky equipment requirements, and challenging
109 deployment in rugged terrain, while also providing only localized data with limited capability to
110 image lateral and deep subsurface structures (Singh, 2005; Lin et al., 2018; Asfahani, 2023).
111 Uncertainty in groundwater resource estimation can arise from the limited availability of
112 borehole data, as the constraints of drilling make it difficult to conduct frequent and widespread
113 borehole investigations. Alternatively, it is essential to develop methods that minimize the

114 reliance on costly drilling while still enabling accurate evaluation of groundwater storage
115 capacity within prospective rock formations.

116 ~~A number of prior groundwater investigations have made use of geophysical techniques (Bentley
117 and Gharibi, 2004; Yadav and Singh, 2007; Fu et al., 2013; Vouillamoz et al., 2014; Robinson et
118 al., 2016; Lin et al., 2018; Kouadio et al., 2020; Abbas et al., 2022; Kouadio et al., 2023; Zhang
119 et al., 2024). A number of studies have shown that geophysical procedures outperform drilling
120 techniques in terms of speed, ease of use, cost, and lack of invasiveness (Hu et al., 2013; Lin et
121 al., 2018; Di et al., 2020; Fusheng et al., 2022; Hasan et al., 2024). Additionally, they are capable
122 of conducting thorough geological evaluations in both the vertical and horizontal planes (Fu et
123 al., 2013; Hasan et al., 2021). These methods are superior to others when it comes to collecting
124 hydrogeological data from various subterranean habitats (Niwas and De Lima, 2003; Wynn et
125 al., 2016; Kouadio et al., 2023). Groundwater studies nowadays often include resistivity surveys.
126 Resistivity methods offer a broader resistivity range compared to other geophysical parameters,
127 which is a major advantage (Bentley and Gharibi, 2004; Camporese et al., 2011; Robinson et al.,
128 2016). The three main methods for measuring resistivity are the controlled source audio-
129 frequency magnetotellurics (CSAMT), vertical electrical soundings (VES), and electrical
130 resistivity tomography (ERT) (Soupios et al., 2007; Di et al., 2020; Zhang et al., 2024). Niwas
131 and De Lima (2003), Soupios et al. (2007), Majumdar and Das (2011), Nwosu et al. (2013),
132 Hasan et al. (2021), and Asfahani (2023) are among the previous groundwater-based geophysical
133 studies that primarily utilized the VES method to evaluate groundwater resources in a single
134 dimension. It is unusual to evaluate aquifer yield at great depths in hard rock terrains using two-
135 and three dimensional hydraulic properties. Recent studies have demonstrated that CSAMT,
136 which aims to gather extensive subsurface data at very deep depths using 2D/3D evaluations, is~~

Formatted: Normal (Web), Indent: First line:
0"

137 ~~the most cost effective and appropriate geophysical method for researching hard rock (Smith and~~
138 ~~Booker, 1991; Simpson and Bahr, 2005; Bai et al., 2010; Fu et al., 2013; Hu et al., 2013; Wang~~
139 ~~et al., 2015; Wynn et al., 2016; Di et al., 2020; Zhang et al., 2021; Kouadio et al., 2023; Hasan et~~
140 ~~al., 2024). Advantages of CSAMT over other geophysical research methods include its lower~~
141 ~~cost, its responsiveness to low resistance rocks, and its ease of usage in challenging topographic~~
142 ~~circumstances (An et al., 2016; Kouadio et al., 2020; Zhang et al., 2021). Compared to most~~
143 ~~geophysical technologies, including ERT, CSAMT's subsurface assessment capabilities are~~
144 ~~superior due to its depth capacity of up to one kilometer (Zonge and Hughes, 1988; Hasan et al.,~~
145 ~~2024). When combined with empirically based methodologies, CSAMT becomes an even more~~
146 ~~powerful tool for studying the incredibly diverse topographical~~ A diverse range of groundwater
147 studies has effectively incorporated geophysical methods to improve subsurface characterization
148 (Bentley and Gharibi, 2004; Yadav and Singh, 2007; Fu et al., 2013; Vouillamoz et al., 2014;
149 Robinson et al., 2016; Lin et al., 2018; Abbas et al., 2022; Kouadio et al., 2023; Zhang et al.,
150 2024). These methods provide notable benefits compared to traditional drilling, especially
151 regarding cost-efficiency, rapid deployment, minimal environmental impact, and ease of field
152 implementation (Hu et al., 2013; Lin et al., 2018; Di et al., 2020; Fusheng et al., 2022; Hasan and
153 Shang, 2022). Geophysical tools offer significant practical advantages, including strong vertical
154 and lateral imaging capabilities, which enhance their effectiveness in capturing the
155 hydrogeological complexity of diverse subsurface conditions (Niwas and De Lima, 2003; Fu et
156 al., 2013; Hasan et al., 2021; Wynn et al., 2016; Kouadio et al., 2023). Resistivity-based methods
157 are pivotal in contemporary groundwater exploration, owing to their sensitivity to diverse
158 subsurface conditions and materials (Bentley and Gharibi, 2004; Camporese et al., 2011;
159 Robinson et al., 2016). The main methods in this category are vertical electrical sounding (VES),

160 electrical resistivity tomography (ERT), and controlled-source audio-frequency magnetotellurics
161 (CSAMT) (Soupios et al., 2007; Di et al., 2020; Zhang et al., 2024). VES has been utilized for
162 one dimensional profiling, especially in areas with horizontally layered aquifers (Niwas and De
163 Lima, 2003; Soupios et al., 2007; Majumdar and Das, 2011; Nwosu et al., 2013; Hasan et al.,
164 2021; Asfahani, 2023). This method is particularly appropriate for small-scale applications (less
165 than 200 m depth), providing low operational costs and reduced logistical requirements.
166 However, its lateral resolution is limited, and its performance can be compromised in
167 geologically complex settings with highly resistive or conductive layers. ERT, by contrast,
168 enables two and three dimensional imaging up to intermediate depths (~300 m) with
169 significantly improved resolution. It is particularly effective for characterizing complex
170 geological settings, such as fractured zones or karst systems, and is widely used for detailed
171 assessments of aquifer geometry and contamination (Bentley and Gharibi, 2004; Camporese et
172 al., 2011; Lin et al., 2018; Abbas et al., 2022; Hasan and Shang, 2022). Nonetheless, it requires
173 greater field effort, careful electrode spacing, and, like VES, may encounter challenges in highly
174 resistive or conductive environments. CSAMT, a more advanced method, is ideally suited for
175 deep investigations (hundreds to thousands of meters), especially in hard rock terrains. It
176 provides two and three dimensional subsurface imaging with strong sensitivity to deep
177 conductive structures, making it highly effective for delineating deep-seated aquifers and
178 geothermal systems (Smith and Booker, 1991; Simpson and Bahr, 2005; Bai et al., 2010; Fu et
179 al., 2013; Hu et al., 2013; Wang et al., 2015; Wynn et al., 2016; Zhang et al., 2021; Kouadio et
180 al., 2023). While CSAMT typically offers lower spatial resolution than ERT, it excels in deep
181 structural mapping, performs well in areas with high cultural noise due to its controlled-source
182 signals, and can be further enhanced when integrated with empirical or model-based approaches

183 (Zonge and Hughes, 1988; An et al., 2016; Hasan et al., 2025). The choice among these
184 resistivity techniques depends on various factors, including investigation depth, target resolution,
185 geological complexity, logistical constraints, cost, field conditions, and resistivity contrast (Di et
186 al., 2020; Hasan and Shang, 2022). Given these considerations, particularly the need to
187 investigate deep aquifer systems in hard rock environments, CSAMT was determined to be the
188 most suitable method for the present study features.

189 ~~Several factors, such as the type of rock, fault, weathering degree, fluid content, permeability,~~
190 ~~pore spacing, fracture, lithology, saturation, and joints, as well as the same structural~~
191 ~~heterogeneities, determine the geophysical and aquifer characteristics (Singh, 2005; Sinha et al.,~~
192 ~~2009; Hasan et al., 2021). Several prior studies utilized geophysical parameters in conjunction~~
193 ~~with hydraulic data or lithological logs to characterize underlying rock mass units~~
194 ~~hydrogeologically (De Lima and Niwas, 2000; Hubbard and Rubin, 2002; Niwas and De Lima,~~
195 ~~2003; Singh, 2005; Soupios et al., 2007; Sinha et al., 2009; Majumdar and Das, 2011; Nwosu et~~
196 ~~al., 2013; Hasan et al., 2021; Asfahani, 2023). Resistivity methods provide an alternate option for~~
197 ~~aquifer parameter estimation by creating a beneficial relationship between electrical resistivity~~
198 ~~and the aquifer parameters (obtained from drilling tests). An innovative aspect of this work is its~~
199 ~~use of non-invasive geophysical techniques to create two and three dimensional k models in a~~
200 ~~diverse environment with a variety of rock types and significant depths. The planned study will~~
201 ~~necessitate the boring of a handful of boreholes at key spots all around the project site. A more~~
202 ~~trustworthy CSAMT study will allow us to evaluate the extensive research area. Then, by~~
203 ~~directly connecting geophysical and borehole data, k can be established for the entire researched~~
204 ~~site, even without drilling tests. Two and three dimensional k models are generated by applying~~
205 ~~the resulting equations to the full study area. This approach would reduce the need for costly~~

206 ~~boreholes to obtain a thorough and complete evaluation of subsurface hydrogeological~~
207 ~~conditions. In fractured rock environments, including granitic, metamorphic, and sandstone~~
208 ~~formations, fluid movement is primarily influenced by the arrangement and connectivity of~~
209 ~~fractures, rather than the inherent porosity of the rock matrix. A precise assessment of hydraulic~~
210 ~~behavior in these environments necessitates the application of integrated methodologies. Recent~~
211 ~~studies emphasize the necessity of integrating geophysical and hydrogeological methods to~~
212 ~~accurately identify and characterize hydraulic properties (McKeown et al., 1999; Medici et al.,~~
213 ~~2023). Interdisciplinary approaches are crucial for improving the precision of flow modeling and~~
214 ~~for guiding groundwater management and geo-energy development in structurally complex~~
215 ~~terrains. Resistivity-based methods are essential in groundwater investigations for their ability to~~
216 ~~delineate subsurface structures and identify areas with water-bearing potential. Recent~~
217 ~~hydrogeophysical studies have focused on the correlation between electrical resistivity and~~
218 ~~permeability, as both are closely related to the fluid content and physical structure of subsurface~~
219 ~~materials. Electrical resistivity, which reflects a material's resistance to the flow of electrical~~
220 ~~current, is influenced by various factors. These include rock type, porosity, weathering extent,~~
221 ~~connectivity of the pore network, saturation level, structural features like faults and fractures, and~~
222 ~~the salinity of pore fluids. Numerous parameters significantly affect permeability, highlighting~~
223 ~~the utility of resistivity measurements as indicators for evaluating groundwater flow potential~~
224 ~~(Singh, 2005; Sinha et al., 2009; Hasan et al., 2021). Numerous studies have investigated~~
225 ~~empirical and semi-empirical correlations between these two parameters, with the objective of~~
226 ~~utilizing resistivity as a proxy for estimating hydraulic conductivity or permeability in regions~~
227 ~~with limited data (De Lima and Niwas, 2000; Hubbard and Rubin, 2002; Niwas and De Lima,~~
228 ~~2003; Singh, 2005; Soupios et al., 2007; Jardani et al., 2007; Sinha et al., 2009; Majumdar and~~

229 Das, 2011; Nwosu et al., 2013; Hasan et al., 2021; Asfahani, 2023). Niwas and De Lima (2003)
230 developed an analytical model linking formation resistivity to transmissivity in porous media.
231 Similarly, Jardani et al. (2007) demonstrated the feasibility of employing geophysical inversions
232 to infer permeability distributions in heterogeneous aquifers. Recent studies have applied these
233 approaches to fractured and hard-rock environments; however, such correlations are less
234 common and frequently constrained by site-specific geological variability (Soupios et al., 2007;
235 Hasan et al., 2021; Asfahani, 2023). Despite recent advancements, the development of robust,
236 high-resolution 2D and 3D permeability models from resistivity data, particularly in geologically
237 complex environments at significant depths, remains a major challenge. To date, no previous
238 studies have successfully achieved this, underscoring the critical need for improved integration
239 of geophysical measurements with sparse borehole data. The relationship between resistivity
240 measurements and borehole-derived data provides an efficient and cost-effective method for
241 estimating aquifer properties over extensive spatial areas and varied depth profiles. This study,
242 for the first time, demonstrates a novel application of the CSAMT technique to create high-
243 resolution two and three dimensional permeability models reaching depths of around 1300 m in a
244 geologically complex and heterogeneous environment characterized by sandstone, granite, and
245 hornstone. A selected number of boreholes were strategically drilled at critical points within the
246 study area. Following this, several CSAMT survey lines were conducted, encompassing both the
247 borehole locations and their surrounding zones. By linking resistivity data from the CSAMT
248 surveys with permeability measurements obtained from borehole core testing, we derived a
249 reliable empirical relationship between resistivity and permeability. This correlation was then
250 applied throughout the entire CSAMT dataset, allowing for the generation of detailed 2D and 3D
251 permeability models even in regions lacking direct borehole data. The method provides a cost-

252 effective and comprehensive framework for evaluating deep groundwater potential, significantly
253 minimizing the reliance on extensive and expensive drilling operations.

254 ~~No one had ever tried to estimate K using direct or indirect methods in such a~~
255 ~~heterogeneous context before this work, where a broad diversity of rock types are present at a~~
256 ~~depth of 1 kilometer. Volumetric measurements of 2D/3D k have never been obtained in hard~~
257 ~~rock exploration using a geophysical technique. Furthermore, no previous research has~~
258 ~~previously derived permeability using the CSAMT method in the same way as this one. Our~~
259 ~~more precise 2D and 3D k model predictions of complex hydrogeological circumstances surpass~~
260 ~~prior investigations, bridging the gap between dependable hydraulic models and limited borehole~~
261 ~~data. The primary goals of this study were as follows: (1) to rapidly predict two and three-~~
262 ~~dimensional k models using geophysical methods; (2) to reliably assess the hydrogeological~~
263 ~~properties of rock formations for deep groundwater assessments in challenging geological~~
264 ~~settings; (3) to minimize costly boreholes and maximize the use of scarce drilling resources to~~
265 ~~collect hydrogeological data over large areas; (4) to decrease uncertainties in hydrogeological~~
266 ~~models; and (5) to promote the use of non-invasive geophysical techniques for hard-rock~~
267 ~~groundwater investigations instead of costly drilling that can damage the rock. This study~~
268 introduces several important advancements in the assessment of deep groundwater resources. It
269 is the first to estimate permeability beyond depths of 1,000 m within a hard-rock environment
270 and to develop detailed two and three dimensional permeability models through geophysical
271 techniques. The innovative use of CSAMT for volumetric hydraulic parameter estimation
272 represents a notable methodological breakthrough. Carried out in a geologically intricate setting
273 dominated by sandstone, granite, and hornstone, where such deep assessments were previously
274 unattempted, this work also highlights the effective integration of limited borehole data to

Formatted: Font: (Default) Times New Roman, 12 pt

Formatted: Font: (Default) Times New Roman, 12 pt

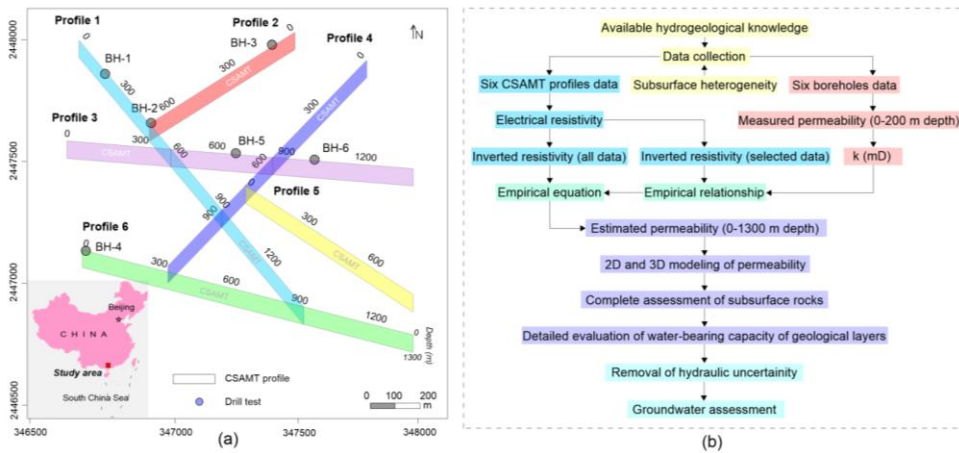
275 generate high-resolution hydrogeological models. This strategy offers a practical and cost-
276 efficient alternative to widespread deep drilling, significantly decreasing the number of boreholes
277 required to achieve similar spatial detail in permeability mapping. The primary aim of this study
278 is to develop and implement a geophysical-based approach for accurately predicting the spatial
279 distribution of permeability in deep, hard rock environments. By integrating CSAMT data with
280 strategically selected borehole measurements, this research enhances the two and three
281 dimensional assessment of hydrogeological properties across various rock types in geologically
282 complex settings, reduces reliance on extensive and costly drilling, and highlights the advantages
283 of using non-invasive geophysical techniques as a more efficient alternative for deep
284 groundwater exploration.

Formatted: Font: (Default) Times New Roman, 12 pt

Formatted: Font: (Default) Times New Roman, 12 pt

285 **2 Methods**

286 This study integrates limited drilling data with the CSAMT method to estimate permeability (k)
287 for both two dimensional and three dimensional assessments of groundwater resources across the
288 entire project area (Fig. 1a). The main stages of the methodology are summarized in the
289 flowchart shown in Fig. 1b.



290

291 **Fig. 1.** (a) Location of the project site, showing six boreholes (BH-1 to BH-6) and six CSAMT survey
 292 profiles (1–6); (b) Flowchart illustrating the methodology for generating 2D and 3D permeability (k)
 293 models to enable comprehensive assessments of groundwater resources across extensive areas

294 **2.1 Study area and hydrogeological settings**

295 ~~This study was conducted in the Jinji region of South China to explore deep underground water~~
 296 ~~sources in a geologically diverse area (Fig. 1a). Due to its monsoon location, the study region~~
 297 ~~experiences a concentration of precipitation in the summer, with an annual precipitation totaling~~
 298 ~~1981 mm. Rivers and other water features surround the Jinji area. The geomorphology of the~~
 299 ~~project site is characterized by low, partly cut, and considerably depleted hills and mountains.~~
 300 ~~The terrain in the north is somewhat flatter than that in the south. At a height of 39 to 447 meters~~
 301 ~~above sea level, the region is famous for a number of characteristics, including a wide range of~~
 302 ~~terrain slopes, from gentle to steep, abundant vegetation, and worn mountain rocks (Yang et al.,~~
 303 ~~2021). Noteworthy among these are Mounts Dashishan, Qilongding, and Jixinshan. The southern~~
 304 ~~part of the research area features the 539.9 meter high Xikeng peak, the landscape's highest~~

305 ~~point. The Yongkouwei River, which flows through the northeastern part of the site under study~~
306 ~~at an elevation of around 7.5 meters, cuts through it. Intruding rocks from the Indosinian,~~
307 ~~Caledonian, and Yanshanian eras are among the many geological formations and periods~~
308 ~~represented in the study region. Other layers from the Paleogene period are also present. The~~
309 ~~most common types of rock that have been discovered are sandstone, granite, and hornstone. The~~
310 ~~complex Kaiping concave fault and fold systems were the dominant geological features in the~~
311 ~~project region, which were developed as a result of magmatic processes and various structures~~
312 ~~(Qin, 2017). Emergence of joint fissured features symbolizes the various tectono-geological~~
313 ~~periods, with the local tectonic line corresponding with the faults strike, especially in the~~
314 ~~northeast orientation (Yang et al., 2021) This study is part of a broader suite of major national-~~
315 ~~level initiatives in South Guangdong of China, each targeting distinct aspects of deep subsurface~~
316 ~~exploration. These include both the investigation of deep groundwater resources, as undertaken~~
317 ~~in this study, and the development of deep-underground engineering infrastructure, such as the~~
318 ~~Jiangmen Underground Neutrino Observatory (JUNO), China's next-generation neutrino detector~~
319 ~~(Hasan et al., 2025). While each project addresses distinct hydrogeological and geotechnical~~
320 ~~challenges, they are collectively aligned with China's broader strategic agenda for deep~~
321 ~~subsurface resource development and sustainable utilization. This study was conducted in the~~
322 ~~Jinji region of South Guangdong, a geologically diverse and structurally complex area prioritized~~
323 ~~for deep groundwater exploration (Fig. 1a). Situated within a subtropical monsoonal climate~~
324 ~~zone, the region experiences intense seasonal rainfall, with an average annual precipitation of~~
325 ~~approximately 1981 mm. The topography is defined by low, eroded hills and moderately~~
326 ~~elevated mountains, with elevations ranging from 39 to 539.9 m above sea level. The study area~~
327 ~~features diverse topography, ranging from mild slopes to sharply inclined terrain, and is~~

328 characterized by dense vegetation cover. The northern portion is comparatively flat, whereas the
329 southern region is more mountainous, distinguished by notable elevations such as Dashishan,
330 Qilongding, Jixinshan, and Xikeng. The Yongkouwei River, located in the northeastern section
331 at approximately 7.5 m above sea level, is a crucial component of the region's surface water
332 drainage system.

333 The Jinji region exhibits a complex geological evolution shaped by various tectono-magmatic
334 events, particularly during the Caledonian (Silurian–Devonian), Indosinian (Late Triassic), and
335 Yanshanian (Jurassic–Cretaceous) orogenic phases. The geodynamic episodes have resulted in a
336 diverse lithological landscape, mainly consisting of granite, sandstone, and hornstone (hornfels)
337 (Qin, 2017; Yang et al., 2021). Extensive granitic intrusions indicate deep crustal magmatism
338 linked to continental collision and subduction processes. Hornstone exemplifies contact
339 metamorphism resulting from the intersection of intrusive bodies with pre-existing sedimentary
340 layers. Paleogene formations, primarily consisting of fluvial and lacustrine deposits, overlay
341 these units and signify a subsequent phase of basin sedimentation. The region is characterized by
342 the Kaiping concave fault-fold system, a significant deformation zone formed through recurrent
343 crustal stress and magmatic processes. This structural framework encompasses various fault
344 types, including reverse, thrust, and strike-slip, indicative of a prolonged history of crustal
345 shortening and lateral displacement. Compressional folds that developed during the Caledonian
346 and Indosinian periods were subsequently modified by strike-slip faulting in the Yanshanian
347 phase. The prevalent northeast-trending orientation of these features aligns with regional stress
348 patterns and significantly influences the subsurface architecture (Qin, 2017; Yang et al., 2021).
349 Fracture networks, consisting of joints and fissures, are widespread in granite, sandstone, and
350 hornstone units. The brittle features, characterized by variations in spacing, orientation, and

Formatted: Indent: First line: 0"

351 continuity based on lithology and structural history, function as essential conduits for
352 groundwater flow. Their spatial alignment with major fault systems highlights a significant
353 relationship between structural geology and hydrogeology, with critical implications for
354 subsurface fluid dynamics in this fractured terrain.

Formatted: Font: Not Bold

355 This study primarily examines the vertical stratification of aquifer-bearing formations in
356 the Jinji region. Highly productive groundwater zones are linked to deeply buried sandstone
357 formations that possess well-developed fracture systems conducive to water storage and flow.
358 The sandstone units are covered by a substantial granite layer with low permeability, which
359 serves as a confining cap that limits vertical recharge from the surface. A hornstone (hornfels)
360 stratum is situated between these two layers, exhibiting intermediate hydraulic properties while
361 providing limited connectivity between the overlying granite and the deeper sandstone. This
362 configuration effectively isolates deep sandstone aquifers from near-surface hydrological
363 processes, making them inaccessible to conventional shallow geophysical or drilling techniques.
364 Targeted deep exploration is essential for the accurate identification and characterization of
365 concealed aquifers, as well as for guiding their sustainable management in this structurally
366 complex hard rock environment.

367 **2.2 CSAMT survey**

368 **2.2.1 Theoretical background**

369 The application of CSAMT in hard rock studies is well documented, as evidenced by various
370 publications (Simpson and Bahr, 2005; Bai et al., 2010; Fu et al., 2013; Wang et al., 2015; Wynn
371 et al., 2016; Di et al., 2020; Zhang et al., 2021; Kouadio et al., 2023; Hasan et al., 2025). In such
372 studies, a distant transmitter emits regulated electric signals into the earth, while a receiving

373 station monitors the electric and magnetic fields (Zonge and Hughes, 1988; Zhang et al., 2021).
374 A mathematical relationship exists between reflection depth and frequency in subsurface
375 structures, where different fields exhibit varied propagation depths (Borah and Patro, 2019). This
376 method utilizes the varying electrical conductivities of different rock types to monitor alterations
377 in magnetic field strength and primary field potential (Cagniard, 1953; Zonge and Hughes,
378 1988). The frequency components of the signal are obtained from the time series of
379 electromagnetic field fluctuations through the application of Fourier transforms (Simpson and
380 Bahr, 2005). A regulated artificial field source is employed in CSAMT. Electrodes positioned
381 one to two kilometers apart can measure the electromagnetic field component of an electric
382 dipole source. The wires connecting the batteries to the current electrodes and the transmitter can
383 be established. The typical distances between field source transmitters and receivers range from
384 5 to 10 km, although this may vary depending on the depth of investigation and geological
385 conditions. A method for determining subsurface resistivity involves calculating the ratio of the
386 magnitudes of the electric and magnetic fields measured in two orthogonal directions. Numerous
387 studies, such as those by Fu et al. (2013), Zhang et al. (2021), and Hasan et al. (2024), have
388 identified various factors affecting resistivity variations in connection with subsurface geological
389 conditions. These factors include lithological variations in stratigraphic structures, fault-induced
390 fragmentation, water saturation, rock types, pore fluid characteristics, and porosity. ~~The vertical~~
391 ~~resolution of 5–20% can be assessed by CSAMT when exploring depths ranging from 20 to 1000~~
392 ~~meters~~ The vertical resolution in CSAMT, indicating the capacity to differentiate between
393 neighboring subsurface layers, generally varies from 5% to 20% of DOI (depth of investigation),
394 which spans approximately 20 to 1000 meters. At shallower depths (e.g., 20–100 m), vertical
395 resolution is higher (closer to 5%), enabling better differentiation between thin layers. At greater

396 depths (up to 1000 m). resolution may degrade toward the 20% mark due to signal attenuation
397 and broader averaging of resistivity data. This makes CSAMT a valuable tool for identifying
398 significant lithological contrasts, fault zones, and resistivity anomalies related to geological
399 structures. The propagation frequency and subsurface resistivity are the basis of DOI. According
400 to Borah and Patro (2019), a lower frequency and higher resistivity typically result in a higher
401 DOI. The distance between stations determines the lateral resolution; typically, this is between
402 ten and two hundred meters. According to Simpson and Bahr (2005), increasing the distance
403 between stations enhances the strength and reliability of the received signal. At every station, a
404 portable receiver processes, amplifies, filters, and records the incoming signal. In order to pick
405 up sent signals, electrode pairs, which include magnetic-field sensors and short grounded
406 dipoles, are utilized. Effective survey planning plays a crucial role in minimizing the impact of
407 metal fence, radio transmitter, power line, and other potential sources of interference that could
408 affect the accuracy of CSAMT data. Plan, three-dimensional, fence, and cross-sectional views
409 are all potential ways to display the modeled resistivity data.

410 2.2.2 Survey design and procedures

411 The CSAMT data was acquired using six profiles (1–6) with a 50 meter interval between each
412 station CSAMT data were collected along six profiles (Profiles 1–6), with a station spacing of 50
413 m between successive measurement points. The selection and location of 6 CSAMT profiles
414 were chosen based on several factors, including geological targets and objectives, surface
415 geology and mapping data, topography and terrain accessibility, orientation relative to structures,
416 spacing and coverage requirements, resistivity contrast expectations, integration with other data
417 (boreholes), environmental and regulatory constraints, and source-receiver geometry
418 requirements, etc. Carefully selected survey profiles enhanced the ability to resolve critical

419 ~~subsurface features and minimized ambiguities in the geophysical interpretation. About 1300~~
420 ~~meters was~~ the depth of investigation (DOI) in the CSAMT ~~investigation~~ survey was about
421 1300 meters. We performed scalar measurements using the Transverse Magnetic (TM) mode,
422 recording bidirectional magnetic and electric field components, both perpendicular and parallel
423 to the survey line. For EMAP observations, measurement stations were arranged sequentially and
424 placed approximately 50 m from the electrodes. The configuration utilized Gain Mode X1 along
425 with a 50 Hz linear filter. Transmission current varied with frequency, ranging from 2.6–4.5 A at
426 7680 Hz to a peak of 12–18 A at 1 Hz. CSAMT data were collected using a V8 multifunction
427 receiver coupled with a TXU-30 transmitter, both produced by Phoenix Geophysics, Canada.
428 The TXU-30 is a versatile, high-power transmitter with a maximum output capacity of 30
429 kilowatts. It enables geophysical operation with transmission voltages up to 1000 V, delivering
430 currents up to 20 A at 1000 V and up to 40 A at 500 V. This GPS-enabled transmitter is ideal for
431 deep investigation since it is compatible with common household three-phase 220 volt
432 alternators. There were 34 separate frequency points utilized, spanning the range of 1–7680 Hz.
433 In addition to collecting data, the V8 multifunction receiver may monitor data sent by other
434 secondary receiving units. The principal receiver's three channels and tracks make this possible.
435 The distances between the transmitter and receiver stations ranged from 9.3 to 12.5 km. Non-
436 polarized electrodes were used to record the electric field signals. Magnetic signals were
437 captured using the AMTC-30 inductive sensor, specifically designed for high-frequency
438 AMT/CSAMT applications, with an operational range from 10,000 Hz to 0.1 Hz. At each site,
439 two orthogonal components of the electric field and three orthogonal components of the
440 magnetic field were acquired, allowing for the computation of the full impedance tensor.
441 Positional data for all measurements were obtained using a Trimble XH dual-frequency GPS

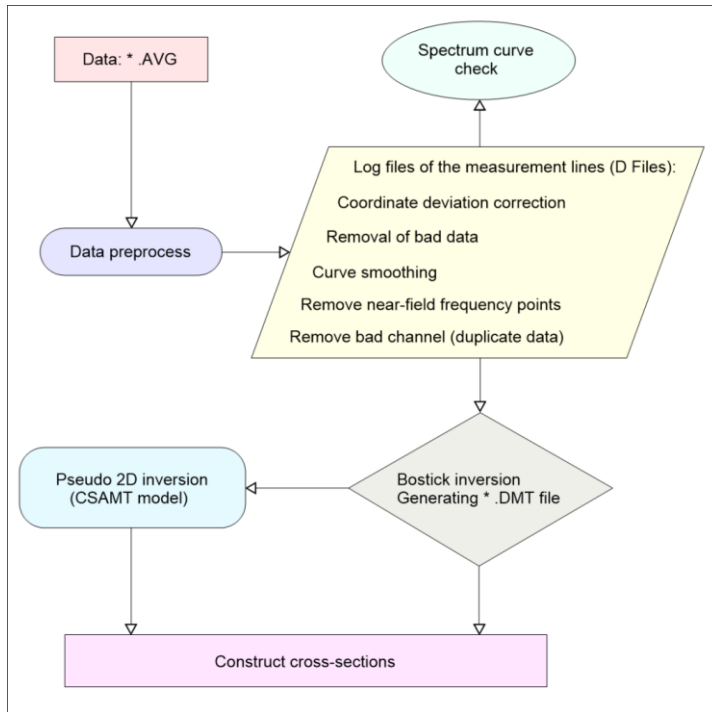
442 receiver, manufactured in the United States. Using the Hi-Tech V30GNSS RTK apparatus, we
443 measured the CSAMT lines for object recognition. Modern navigational aids allow for pinpoint
444 accuracy on the order of sub-meter precision. The computer calculated the coordinate values of
445 each survey line and survey point using the given direction and distance, and then sent them to
446 the GPS or RTK. Survey line measurement points were identified using RTK or GPS navigation
447 systems. The spatial distribution of inspection points was consistently maintained, with system
448 quality assessments showing variability within a 3–5% range along the measurement lines. The
449 system quality assessment met the following design criteria: a root-mean-square (RMS) error of
450 less than $\pm 5\%$, an allowable error of less than 10 between consecutive profile points, a relative
451 elevation tolerance of 1.67 mm, and a planar tolerance of 2.33 mm. Due to the absence of
452 anthropogenic and electrical interference at the survey site, the collected data was of
453 exceptionally high quality. Site characteristics were interpreted based on the analysis of the
454 CSAMT data (An and Di, 2016; Hasan et al., 2025). After eliminating skewed data, a detailed
455 curve analysis was performed. ~~The static corrections were made using a Hanning window spatial
456 filtering method, which involved geological information and curve analysis. Correct data
457 processing and interpretation were thus facilitated by the availability of high quality geophysical
458 data.~~

459 2.2.3 Processing workflow

460 Static correction and spatial filtering using a Hanning window are essential preprocessing steps
461 in CSAMT data analysis, aimed at improving data quality and enhancing the reliability of
462 subsurface resistivity models. Static correction mitigates the impact of near-surface resistivity
463 inhomogeneities, which can distort electric field measurements and result in static shifts, leading
464 to vertical displacements in apparent resistivity curves that misrepresent deeper subsurface

465 conditions. To improve data quality, measured electric fields were calibrated against a stable
466 baseline or averaged field, thereby reducing the impact of shallow subsurface layers and isolating
467 signals from deeper sources. Simultaneously, spatial filtering techniques were employed to
468 mitigate noise resulting from environmental and instrumental interference. The Hanning (Hann)
469 window demonstrated notable effectiveness in suppressing spectral leakage and smoothing
470 fluctuations while preserving underlying trends. The Hanning window, when applied in spatial
471 filtering, executed weighted averaging among adjacent measurement stations, preserving
472 coherent spatial patterns and reducing high-frequency noise. This method markedly enhanced the
473 stability and interpretability of the resulting inversion models. For the data processing step, we
474 used the CMTPro Version software produced by Phoenix Geophysics (Phoenix Geophysics
475 CMTPro, 2020). This program combines V8 and tracking data, and source current into CMT
476 files, corrects electrode coordinates, automatically smoothes observed curves, and generates files
477 in the AVG format, among other things. Fig. 2 shows a flow diagram of the CSAMT-SW
478 method (Phoenix Geophysics CSAMT-SW, 2020) that was used to conduct the 2D inversion
479 (Rodi and Mackie, 2001; Wang et al., 2015).

Formatted: Font: (Default) Times New Roman, 12 pt, Not Bold

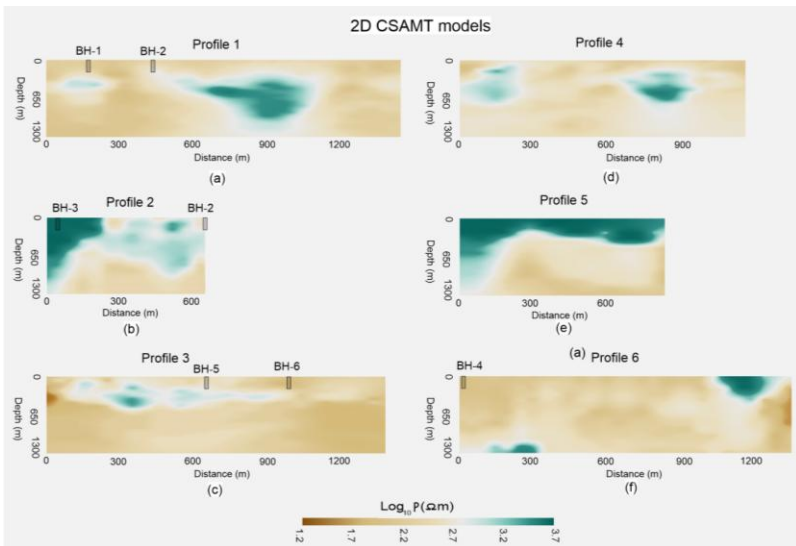


480

481 **Fig. 2.** Illustration of the 2D inversion process of CSAMT data using Bostick inversion

482 Here are the main components of the CSAMT-SW: 1. Data format conversion from AVG
 483 to D; 2. Editing and generating CHK elevation files, and converting them to format D; 3.
 484 Manually checking the file D for corrupted sectors, filling in the gaps, removing near-field data,
 485 and skipping to certain spots; 4. Inversion outcomes from different static correction methods
 486 were very similar when compared; the D file was utilized for smoothing processing; 5. D, H, K,
 487 and Z are the four static correction results files for various correction approaches; 6. Generating
 488 text files through BOSTICK inversion combined with near-field correction; 7. Using quasi-2D
 489 inversion combined with the CSAMT global field model (ID), which integrates both near and
 490 transition fields, finite-depth layers representing resistivity variations can be generated directly

491 from the measured CSAMT data. After applying Bostick inversion (Fusheng et al., 2022), the
492 output data in D format were saved as *_BOS.DAT and *_BSS.DAT files, respectively. The
493 processed data, formatted according to the requirements of the CSAMT 2D inversion model,
494 were stored in a newly created *_M.DMT text file. The inversion process continued until either
495 the maximum number of iterations, set at five, or the target RMS error was reached. At this point,
496 the resulting models were fitted to the observed data using the inversion method. A trustworthy
497 2D resistivity model (Zhang et al., 2021) of CSAMT was produced, considering the local
498 geology and dataset quirks, by employing the most appropriate processing and inversion
499 procedures to reduce model errors. The final inversion models (Fig. 3), through delineation of
500 resistivity variations, significantly enhanced our understanding of the subsurface geological
501 framework.



502

503 **Fig. 3.** Construction of 2D CSAMT models along six geophysical profiles: (a) Profile 1, (b) Profile 2, (c)
504 Profile 3, (d) Profile 4, (e) Profile 5, and (f) Profile 6. Resistivity values increase from brown to green on
505 the color scale.

506 2.3 Permeability estimation framework

507 2.3.1 Laboratory-based permeability determination from borehole core samples

Formatted: Font: (Default) Times New Roman, 12 pt

508 Permeability (k) is a fundamental hydrogeological parameter that describes the capacity of a
509 porous medium, such as rock or sediment, to transmit water. This concept is crucial for
510 comprehending fluid dynamics in aquifers and is extensively utilized in groundwater evaluations
511 (Allègre et al., 2016; Fiandaca et al., 2018; Mudunuru et al., 2022; Esmailpour et al., 2023;
512 Carbillet et al., 2024). The permeability of a formation indicates the extent to which fluids can
513 move through pore spaces or interconnected fractures, serving as a critical factor in subsurface
514 hydrodynamics at different depths. K is typically determined via pumping tests or direct testing
515 of rock cores collected from boreholes, a method that is both expensive and logistically
516 demanding. Permeability is affected by various geological and physical factors, including
517 porosity, lithological composition, saturation level, faulting, jointing, and diagenetic processes
518 such as compaction and mineral alteration (Dewandel et al., 2006; Yan et al., 2024).

519 In this study, the initial permeability data from the Jinji region were limited to just six boreholes.
520 A suite of laboratory analyses was conducted on rock core samples obtained from the deep
521 boreholes to enhance the dataset's robustness. The research concentrated on three primary
522 lithologies: sandstone, hornstone (hornfels), and granite. The samples covered depths reaching
523 200 m. A total of 116 laboratory measurements were collected, comprising 31 from sandstone,
524 23 from hornstone, and 62 from granite. These measurements offer significant insights into the

Formatted: Justified, Line spacing: Double

525 vertical distribution of permeability across various strata, thereby enhancing the hydrogeological
526 characterization of the region (Neuzil, 1994; Zhang et al., 2020).

527 Coring was performed utilizing a wireline rotary system equipped with triple-tube barrels to
528 achieve minimal disturbance and optimal recovery of intact samples (ISRM, 2007). Core
529 samples were promptly vacuum-sealed and stored under controlled humidity to maintain in-situ
530 moisture conditions and the integrity of microfracture networks. Before testing, cores were
531 sectioned into standardized cylindrical specimens, generally measuring 50 mm in diameter and
532 100 mm in length, and examined to eliminate any visibly fractured or altered areas.

533 Two distinct laboratory techniques were utilized according to the anticipated permeability range
534 of each rock type. A steady-state flow method was employed for sandstone, which typically
535 demonstrates higher permeability, in accordance with ASTM D5084-21 guidelines (ASTM,
536 2021). A constant hydraulic gradient was applied under fully saturated conditions, and the
537 corresponding volumetric flow rate was recorded. Permeability was determined through the
538 application of Darcy's Law:

Formatted: Normal (Web), Indent: First line: 0", Space Before: 0 pt, After: 0 pt

539
$$k = \frac{Q \cdot \mu \cdot L}{A \cdot \Delta P} \quad (1)$$

Formatted: Font: Not Bold, Not Italic

540 where Q is the flow rate (m^3/s), μ is the fluid viscosity ($\text{Pa}\cdot\text{s}$), L is the sample length (m), A is the
541 cross-sectional area (m^2), and ΔP is the applied pressure difference (Pa).

Formatted: Justified, Line spacing: Double

542 The transient pulse decay method was employed for granite and hornstone, both of which exhibit
543 low permeability, adhering to the procedure originally outlined by Brace et al. (1968) and
544 subsequently refined by Hsieh et al. (1981). This method involves introducing a brief pressure
545 pulse at one end of the saturated specimen and monitoring the rate of pressure decay over time.

546 Tests were performed under confining pressures reaching 30 MPa to replicate in-situ stress
547 conditions and to examine the stress-sensitive behavior of crystalline rocks, where fracture
548 closure can notably influence permeability (Faybishenko et al., 2000; Niu et al., 2016).

549 Each lithology underwent testing under both dry and saturated conditions to assess the influence
550 of moisture content on permeability. Measurements were replicated to ensure data reliability, and
551 statistical analyses were employed to evaluate variability within and among lithological groups
552 (Zhao et al., 2018). The permeability data were organized by depth and lithology to create
553 vertical permeability profiles, which served as a crucial input for analyzing the
554 hydrostratigraphic framework of the subsurface. Granite demonstrated the lowest permeability,
555 indicative of its dense, unfractured crystalline structure. Hornstone exhibited intermediate
556 permeability values, probably resulting from localized tectonic or thermally induced fractures.
557 Conversely, sandstone layers at increased depths exhibited markedly higher permeability,
558 aligning with their function as the primary aquifer units in the study region (Wang et al., 2014;
559 Liu et al., 2021).

Formatted: Normal (Web), Indent: First line: 0"

560 2.3.2 Permeability-resistivity relationship (Archie and Kozeny-Carman equation)

561 Several foundational studies have established empirical and theoretical relationships between
562 electrical resistivity and hydraulic properties such as permeability. The Archie equation,
563 introduced by Archie (1942), is widely used in clean, saturated sedimentary formations. It relates
564 formation resistivity to porosity and water saturation but assumes the absence of clay minerals
565 and thus has limitations in more complex lithologies (Waxman & Smits, 1968; Glover, 2015).
566 The Kozeny-Carman equation is another widely accepted model that links permeability to
567 porosity and specific surface area (Bear, 1972; Carman, 1956). While it does not directly involve

Formatted: Font: (Default) Times New Roman, 12 pt, Not Bold

Formatted: Font: (Default) Times New Roman, 12 pt, Not Bold

568 resistivity, it is often used alongside petrophysical models to interpret hydrogeological
569 characteristics based on geophysical data (Paterson & Wong, 2005; Clennell, 1997).

Formatted: Font: (Default) Times New Roman, 12 pt, Not Bold

570 Archie's law (Archie, 1942) relates the bulk electrical resistivity of a fully saturated porous
571 medium to its porosity and fluid resistivity. It is commonly expressed as:

$$572 \rho_b = a \cdot \rho_f \cdot \phi^{-m} \quad (2)$$

573 where, ρ_b is the bulk resistivity, ρ_f is the fluid resistivity, ϕ is the porosity, a and m are empirical
574 constants. Although Archie's law does not directly estimate permeability, porosity is often used
575 as a proxy because of its influence on fluid flow. The resistivity-porosity relationship can be
576 indirectly extended to infer permeability, especially when combined with other petrophysical
577 models (Binley et al., 2005; Revil & Cathles, 1999).

Formatted: Font: (Default) Times New Roman, 12 pt, Not Bold

578 The Kozeny-Carman equation establishes a theoretical relationship between permeability (k) and
579 porosity (ϕ), expressed as follows:

$$580 k = \frac{C \cdot \phi^3}{(1-\phi)^2 \cdot S^2} \quad (3)$$

581 In this equation, k denotes permeability, ϕ represents porosity, S is the specific surface area, and
582 C is a structural constant reflecting pore geometry and tortuosity. The application of this
583 equation alongside Archie's law facilitates the development of empirical or semi-empirical
584 models that connect electrical resistivity to permeability (Jiang et al., 2014; Jardani et al., 2007).

Formatted: Justified, Line spacing: Double

585 Although these formulations offer a robust theoretical foundation, their direct application in
586 complex geological contexts, particularly in heterogeneous hard rock such as granite, sandstone,
587 and hornstone, is frequently limited. This results mainly from differences in mineral

Formatted: Normal (Web), Indent: First line: 0"

588 composition, pore connectivity, and structural anisotropy (Roa-García et al., 2010; Singh et al.,
589 2020). Our present study establishes a localized empirical relationship between resistivity and
590 permeability through co-located measurements obtained from deep boreholes and CSAMT
591 profiles to address these challenges. Such correlation facilitates the development of high-
592 resolution 2D and 3D permeability models in the Jinji area (study area), thereby improving the
593 comprehension of subsurface hydrogeology in contexts where traditional methods fall short.

594 **2.3.3 Spatial permeability modeling from CSAMT data**

595 ~~A large number of researchers have found substantial evidence that geophysical and~~
596 ~~hydrological features are correlated (De Lima and Niwas, 2000; Hubbard and Rubin, 2002;~~
597 ~~Niwas and De Lima, 2003; Singh, 2005; Soupios et al., 2007; Sinha et al., 2009; Majumdar and~~
598 ~~Das, 2011; Asfahani, 2023). The first step in establishing these connections is to calculate the~~
599 ~~permeability using drilling data collected at certain points. The next step is to integrate the~~
600 ~~electrical resistivity (using geophysical data) and permeability (measured in boreholes) in order~~
601 ~~to derive the empirical equations. After that, we put all of the resistivity readings from the six~~
602 ~~profiles into the resulting equation to get the overall site permeability. This makes it possible to~~
603 ~~find the site's complete permeability, even when a borehole is inaccessible. In order to provide a~~
604 ~~one dimensional estimate of permeability, most of the earlier empirical geophysical approaches~~
605 ~~relied on vertical electrical sounding (VES), which was most common in uniform settings at~~
606 ~~shallow depths. As a result, no one had ever used k to probe deep underground water, especially~~
607 ~~in hard rock formations. We used a CSAMT based empirical approach to estimate two and three~~
608 ~~dimensional k across a vast area with different rock formations at great depths for the first time~~
609 ~~in our recent research.~~

Formatted: Font: (Default) Times New Roman, 12 pt

Formatted: Font: Bold

610 Initially, 37 k measurements were obtained from six boreholes (W1, W2, W3, W4, W5,
611 and W6) at varying depths ranging from 10 to 200 meters (Fig. 3a). In the second stage, 37
612 borehole-derived k values were empirically correlated with 37 resistivity values from the chosen
613 CSAMT soundings. P1-5 represents the fifth sounding at 200 meters on surveyed line 1 with
614 well W1; P1-9 denotes the ninth sounding at 400 meters along profile 1 with well W2; P2-3
615 indicates the third sounding at 100 meters with profile 2 and well W3; P6-1 signifies the first
616 sounding at 0 meters on surveyed line 6 with well W4; P3-15 refers to the fifteenth sounding at
617 700 meters along profile 3 with well W5; and P3-21 corresponds to the twenty-first sounding at
618 1000 meters on surveyed line 3 with well W6. In the third stage, the empirical integration of the
619 selected observations (37 data sets) of CSAMT-based resistivity and borehole-based k was
620 utilized to formulate the subsequent equation (Fig. 3b):

$$k = 15.345(e)^{-0.002(\rho)} \quad (1)$$

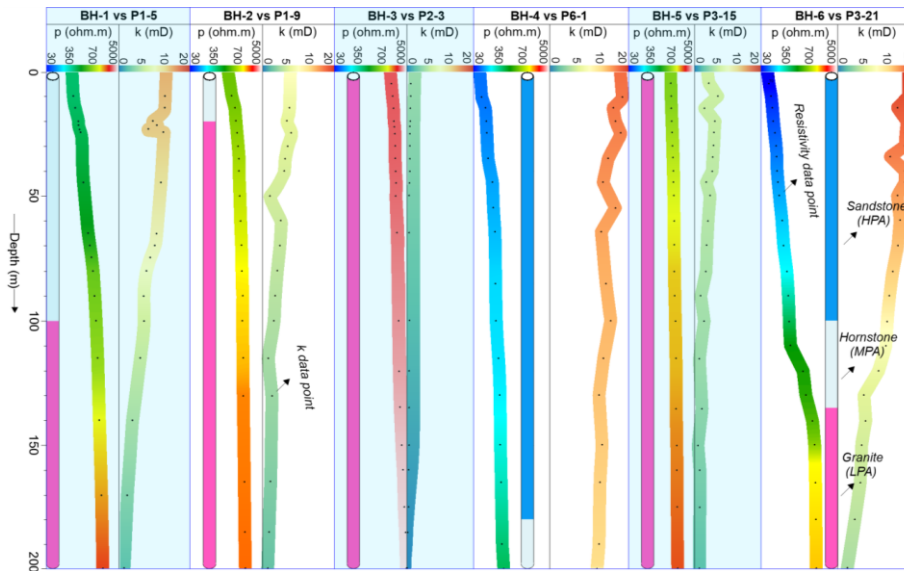
621 where k stands for permeability, which is measured in m/d units, and ρ signifies the true
622 or inverted resistivity, denoted in Ωm . Using comprehensive resistivity data from six geophysical
623 surveyed lines, Eq. (1) was used to predict permeability (k) over the entire area. In this way, we
624 were able to assess the water-retaining capacity of three rock types: granite, hornstone, and
625 sandstone. This allowed us to conduct a thorough evaluation of groundwater resources from 0 to
626 1300 meters below the surface across three potential aquifers: low potential aquifer (LPA)
627 connected to granite, medium potential aquifer (MPA) contained inside hornstone and high
628 potential aquifer (HPA) linked to sandstone). Finally, two and three-dimensional models were
629 created using the Geosoft and SKUA-GOCAD software tools for the k parameter, a predicted
630 hydrogeological feature that extends throughout all 1-6 geophysical profiles (Webring, 1981;
631 Mira Geoscience Ltd, 1999; Hasan et al., 2024)
632

Formatted: Justified, Indent: First line: 0.5", Space After: 0 pt

Formatted: Indent: First line: 0.5", Space After: 0 pt

633 To estimate permeability (k) across the entire study area, we implemented a multi-stage
634 approach integrating borehole core analysis with CSAMT-derived resistivity data. In the first
635 stage, a total of 116 laboratory-based permeability measurements were acquired from six
636 boreholes (from BH-1 to BH-6), drilled to depths ranging from 0 to 200 m (Fig. 4). These
637 measurements were obtained from intact rock core samples representing three principal
638 lithologies: granite, hornstone, and sandstone.

639 In the second stage, each of the 116 borehole-derived k values was empirically correlated
640 with corresponding resistivity values extracted from CSAMT soundings co-located with the
641 borehole sites. The spatial correspondence between boreholes and CSAMT sounding points was
642 carefully matched (Fig. 4). For example: P1-5 represents the fifth CSAMT sounding at 200 m
643 along survey line 1 near borehole BH-1; P1-9 corresponds to the ninth sounding at 400 m on line
644 1 near borehole BH-2; P2-3 denotes the third sounding at 100 m along line 2 near BH-3; P6-1
645 indicates the first sounding at 0 m on line 6 adjacent to BH-4; P3-15 and P3-21 represent the
646 fifteenth (700 m) and twenty-first (1000 m) soundings along line 3, near boreholes BH-5 and
647 BH-6, respectively.



648

649 **Fig. 4.** Comparison of 116 CSAMT-based resistivity (ρ) data points with corresponding drilling-based
 650 permeability (k) values at depths of 0–200 m across six borehole locations (BH-1 to BH-6). The data were
 651 used to evaluate high potential aquifers (HPA) in sandstone, medium potential aquifers (MPA) in
 652 hornstone, and low potential aquifers (LPA) in granite. Each dot represents a resistivity or permeability
 653 data point. Sounding labels indicate specific CSAMT locations: P1-5 (5th point on Line 1), P1-9 (9th on
 654 Line 1), P2-3 (3rd on Line 2), P6-1 (1st on Line 6), and P3-15 and P3-21 (15th and 21st on Line 3.)

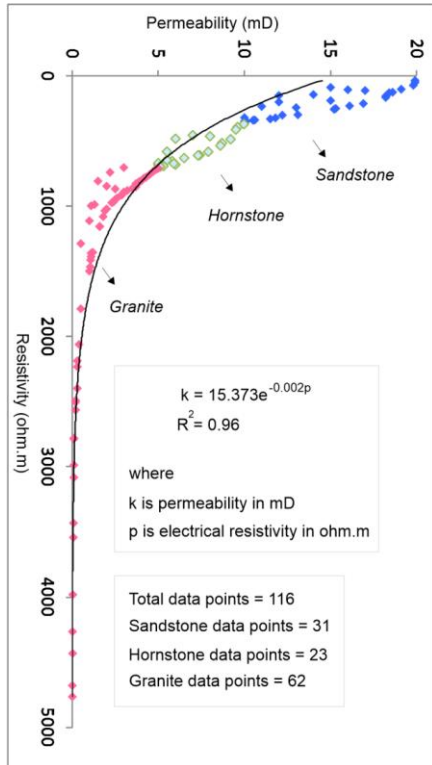
655 In the third stage, all 116 paired measurements of permeability (k) and resistivity (ρ)
 656 were utilized to develop an empirical model. An exponential relationship was derived between
 657 permeability (k in millidarcies or mD) and electrical resistivity (ρ in Ω m), expressed as follows
 658 (Fig. 5):

Formatted: Font: 12 pt, Not Bold

659
$$k = 15.373(e)^{-0.002(\rho)} \quad (4)$$

660 This site-specific empirical model was then applied to the entire suite of CSAMT resistivity data
661 collected along six survey profiles to estimate spatial variations in permeability across the
662 broader study area. Using this relationship, we generated predictive 2D and 3D permeability
663 models that capture the hydraulic behavior of three major lithological units: low potential aquifer
664 (LPA): associated with low-permeability granite, medium potential aquifer (MPA): hosted
665 within fractured hornstone (hornfels), high potential aquifer (HPA): corresponding to more
666 porous sandstone units.

667 These models provide a depth-resolved assessment of subsurface permeability from the surface
668 down to approximately 1300 m. Final 2D and 3D spatial visualizations were developed using
669 Geosoft Oasis montaj and SKUA-GOCAD modeling platforms (Webring, 1981; Mira
670 Geoscience Ltd., 1999; Hasan et al., 2024), enabling the visualization of permeability
671 distributions across all six CSAMT profiles and improving hydrogeological characterization in
672 structurally complex hard rock terrain.



673

674 **Fig. 5.** Empirical relationship derived from 116 data points comparing CSAMT-based resistivity and
 675 drilling-based permeability at depths of 0–200 m, across three lithologies: sandstone (31 data points),
 676 hornstone (23 data points), and granite (62 data points).

677 **3 Results**

678 **3.1 Cross-validation of geophysical and borehole parameters**

679 **Table 1** summarizes the integrated dataset from six boreholes and six CSAMT profiles, which
 680 were used to delineate the subsurface into three distinct hydrogeological units, based on
 681 variations in electrical resistivity and corresponding permeability (k) values. The development of

682 these subsurface models mainly depends on borehole data, CSAMT-derived resistivity
 683 measurements, and the regional geological framework. The stratigraphy was categorized into
 684 three primary lithologies: sandstone, hornstone, and granite. Classification criteria were
 685 established as follows: sandstone was defined by resistivity values below 350 Ωm and a
 686 permeability range of 10–20 m/dmD ; hornstone exhibited resistivity values between 350 and 700
 687 Ωm with a k range of 5–10 m/dmD ; and granite was characterized by resistivity values
 688 exceeding 700 Ωm and permeability values ranging from 0 to 5 m/dmD . Based on our
 689 evaluations of the subsurface hydrogeological model's aquifer potential zones, we found that
 690 sandstone contains the high potential aquifer (HPA), hornstone contains medium potential
 691 aquifer (MPA), and granite has low potential aquifer (LPA). Aquifers with the largest yields or
 692 the best water-bearing capacity are indicated by sandstone, whereas aquifers with the lowest
 693 yields or the worst water-bearing capacities are denoted by granite. Groundwater development is
 694 best facilitated by sandstone in the study area, whereas groundwater extraction is most hindered
 695 by granite.

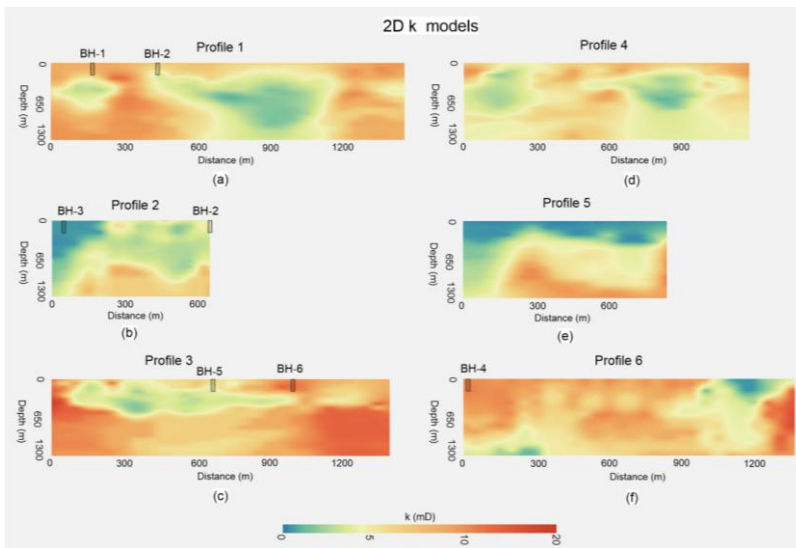
696 **Table 1**

697 Integrating distinct ranges of electrical resistivity and permeability (k) enables a comprehensive
 698 assessment of groundwater potential across various hard rock types

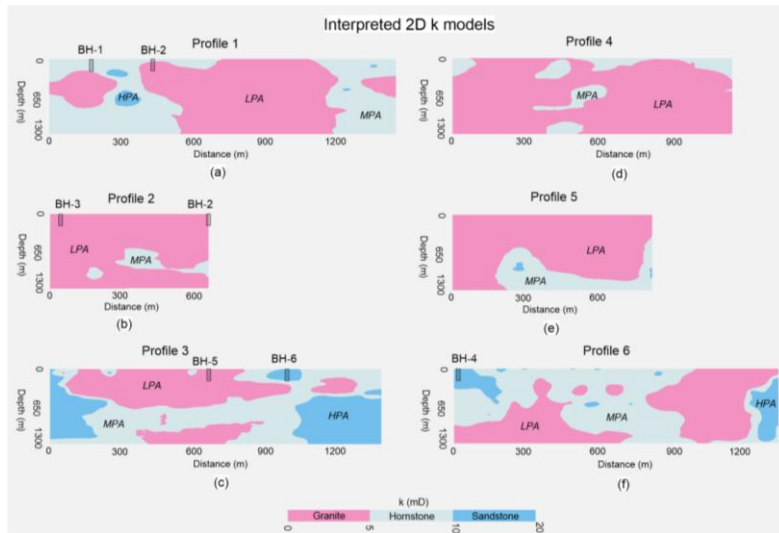
Resistivity (Ωm)	k (m/dmD)	Type of rock	Aquifer potential
< 350	10–20	Sandstone	High potential aquifer (HPA)
350–700	5–10	Hornstone	Medium potential aquifer (MPA)
>700	0–5	Granite	Low potential aquifer (LPA)

699 **3.2 2D groundwater assessments**

700 Using geophysical-borehole correlation as its basis, Eq. (4) efficiently converts two dimensional
701 CSAMT models (Fig. 3) into two dimensional k models (Fig. 6). The interpreted 2D k models
702 shown in Fig. 7, in comparison with the limited borehole experiments, allow for an accurate and
703 comprehensive assessment of the groundwater resources in hard rock across the whole research
704 area, from 0 to 1300 m deep.



705
706 **Fig. 6.** The predicted 2D k models along six geophysical profiles: (a) Profile 1, (b) Profile 2, (c) Profile 3,
707 (d) Profile 4, (e) Profile 5, and (f) Profile 6. k values increase from blue to red on the color scale.



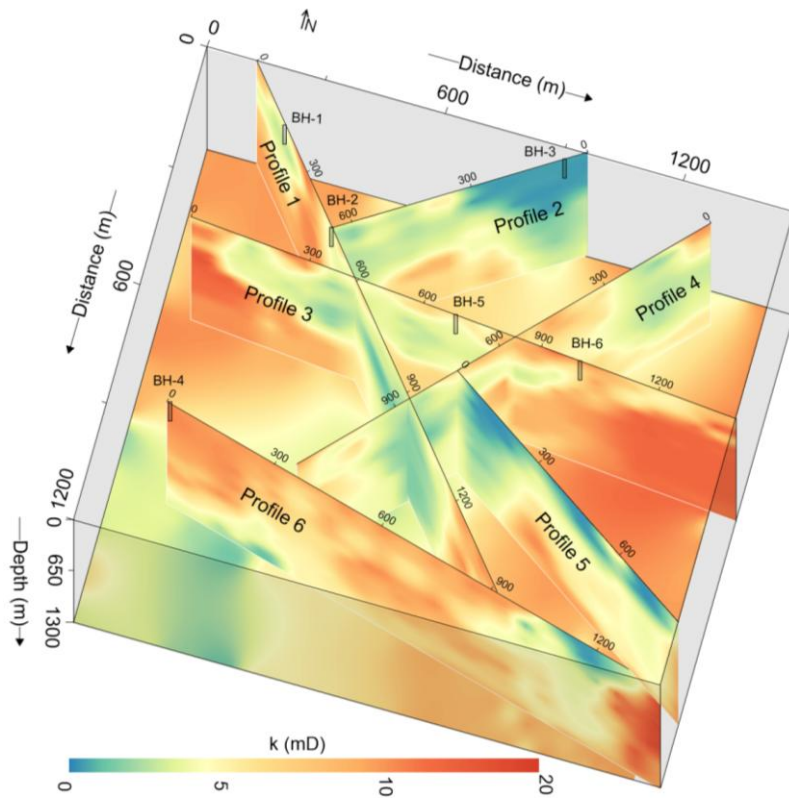
708

709 **Fig. 7.** The interpretation of the predicted 2D k models along six geophysical profiles: (a) Profile 1, (b)
 710 Profile 2, (c) Profile 3, (d) Profile 4, (e) Profile 5, and (f) Profile 6. Sandstone is represented in blue,
 711 hornstone in light blue, and granite in pink

712 The integrated 2D k models (Fig. 8) and their interpretation (Fig. 9) offers a more
 713 comprehensive and detailed two dimensional evaluations of groundwater resources within the
 714 highly heterogeneous geological settings of sandstone, hornstone, and granite. Line 1 of the
 715 survey has had the following geological layers marked out for the purpose of groundwater
 716 evaluation: A sandstone layer of high potential aquifer, 85 to 305 m thick, is visible between 245
 717 and 380 m of distance, at depths ranging from 205 to 400 m. From 0 to 1300 m below surface, at
 718 concentrations of 0 to 525 m and 1185 to 1445 m away, the remaining portion of the profile is
 719 composed of a medium potential aquifer embedded in sandstone. Distances of 0–285 m within
 720 290–790 m depth, 385–1185 m between 0–1300 m depth, and 1305–1450 m within 390–745 m
 721 depth were used to assess granite aquifers with poor potential. Along profile 2, the geological

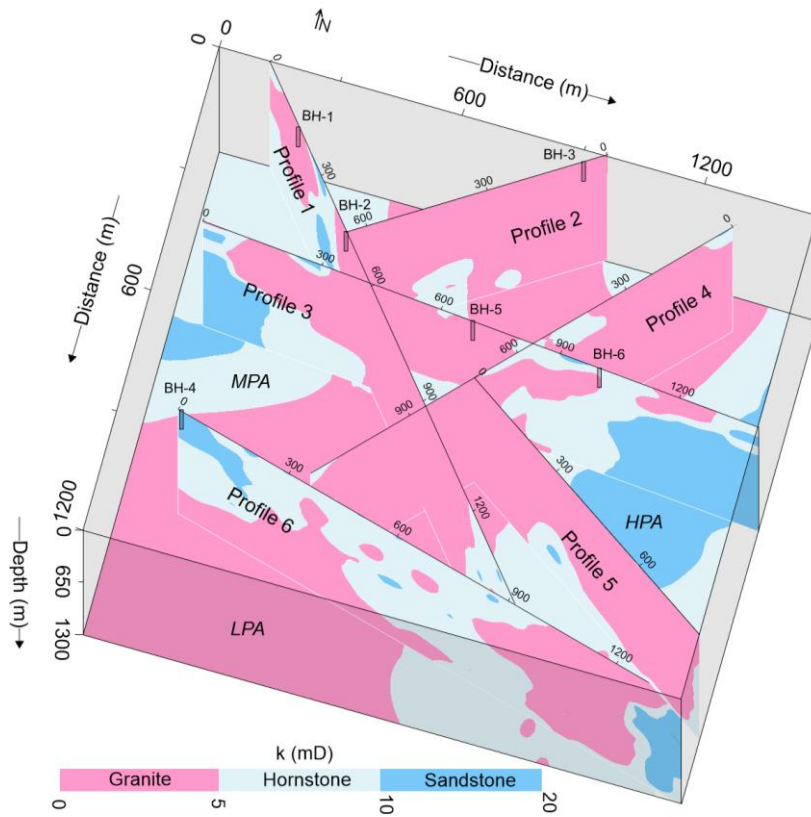
722 layers that were employed for groundwater assessment are described as follows: A hornstone
723 layer 140–380 m thick encloses a medium potential aquifer 490–1105 m below ground, more
724 precisely between 145–215 m and 290–645 m distance. We did not detect any sandstone
725 associated with the high potential aquifer along this profile. Along this profile, granite from low
726 potential aquifers predominates, with the exception of the zones evaluated by medium potential
727 hornstone aquifers; granite is located at 0–700 m distance between 0–1300 m depths. Along
728 profile 3, the following geological layers have been characterized for the purpose of groundwater
729 evaluation: A hornstone-containing medium potential aquifer is evaluated at depths between 0
730 and 1300 m and within a range of 0 to 1400 m distance. Sandstone-associated high potential
731 aquifers are located between 0 and 250 m distance and between 0 and 1190 m depths; 905 and
732 1065 m away between 0 and 205 m deep; and 1040 and 1390 m distance and between 490 and
733 1305 m depths. Distances of 80–1015 m between 0–590 m depths, 395–845 m between 915–
734 1300 m depth, and 1100–1300 m between 200–500 m depth are used to assess the possible
735 aquifers contained beneath granite. Here is the breakdown of the geological layers in profile 4 for
736 the purpose of groundwater assessment: The hornstone medium potential aquifer is checked at
737 distances of 0–105 m and depths of 0–340 m. There is a layer about 290 m thick hornstone at 0–
738 1300 m depth between 340 and 645 m distances, with depths of 0–300 m between 595 and 790
739 m profile spread, and 0–345 m deep between 1015 and 1145 m distance. No sandstone that could
740 contain a high potential aquifer is being investigated along this profile. The low potential aquifer
741 associated with granite is delineated at most portions of the profile at 0–1145 m distance between
742 0–1300 m depths, excluding the areas with medium potential aquifer of hornstone. The
743 geological layers that were considered for the groundwater assessment along profile 5 are as
744 follows: Between 190 and 845 m beneath the granite, there is hornstone associated with a

745 medium potential aquifer, which is located between 390 and 1325 m below the surface. Two
746 small sandstone patches of high yield aquifer can also be seen along this profile. One is at 790–
747 960 m depth for 290 m distances, while the other is at 815 m, between 1045 and 1135 m depth.
748 Within the depth range of 0–1300 m, granite from low potential aquifers is assessed at a distance
749 of 0–190 m, and between 0 and 1025 m, at a distance of 790–815 m. Here are the geological
750 layers that can be used for groundwater assessment along profile 6: To assess the high potential
751 aquifer linked to sandstone, distances of 0–190 m between depths of 0–490 m and 1245–1345 m
752 between depths of 215–1225 m are utilized. Distances of 0–690 m within depths of 390–1300 m
753 and 790–1360 m within 0–1190 m depths are used to evaluate low yield aquifer granite. Between
754 0 and 1300 m depth and 0 and 1350 m distance, the hornstone of the medium potential aquifer
755 dominates the rest of the profile. In the southeastern and northwest regions, there are a lot of
756 medium to high potential aquifers, according to the results of the integrated 2D k models shown
757 in [Fig. 8](#) and [9](#). On the other hand, in the central areas, groundwater resources are scarce or
758 nonexistent.



759

760 **Fig. 8.** The integrated 2D k models derived from the incorporation of geophysical and drilling data, with k
 761 represented on a color bar spanning from green to red



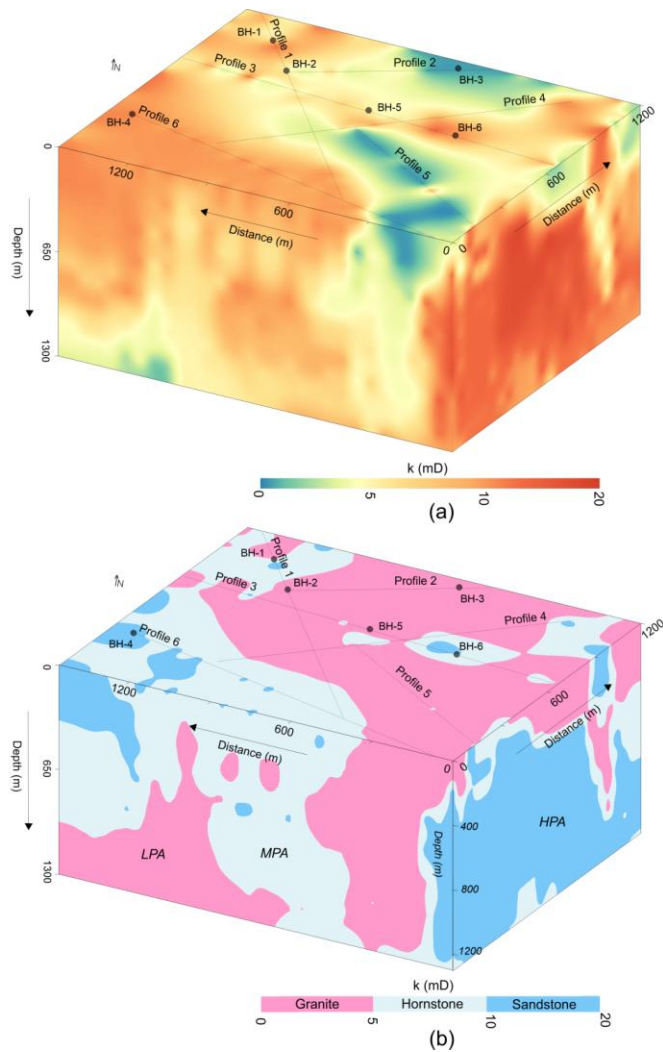
762

763 **Fig. 9** Analysis of 2D permeability (k) models, based on defined k ranges, for three groundwater potential
 764 aquifers: low potential aquifer (LPA), medium potential aquifer (MPA), and high potential aquifer (HPA),
 765 corresponding to the granite, hornstone, and sandstone formations, respectively

766 **3.3 3D groundwater assessments**

767 A thorough assessment of the water-bearing capacity of the rock mass for groundwater
 768 evaluation was conducted using the 3D k external visualization depicted in Fig. 10 (a, b). The
 769 granite of low potential aquifer was evaluated at the ground surface along profile 1 at distances
 770 of 85–215 m and 385–1175 m, surveyed line 2 at 0–655 m, CSAMT line 3 at 0–45 m, 95–175 m,

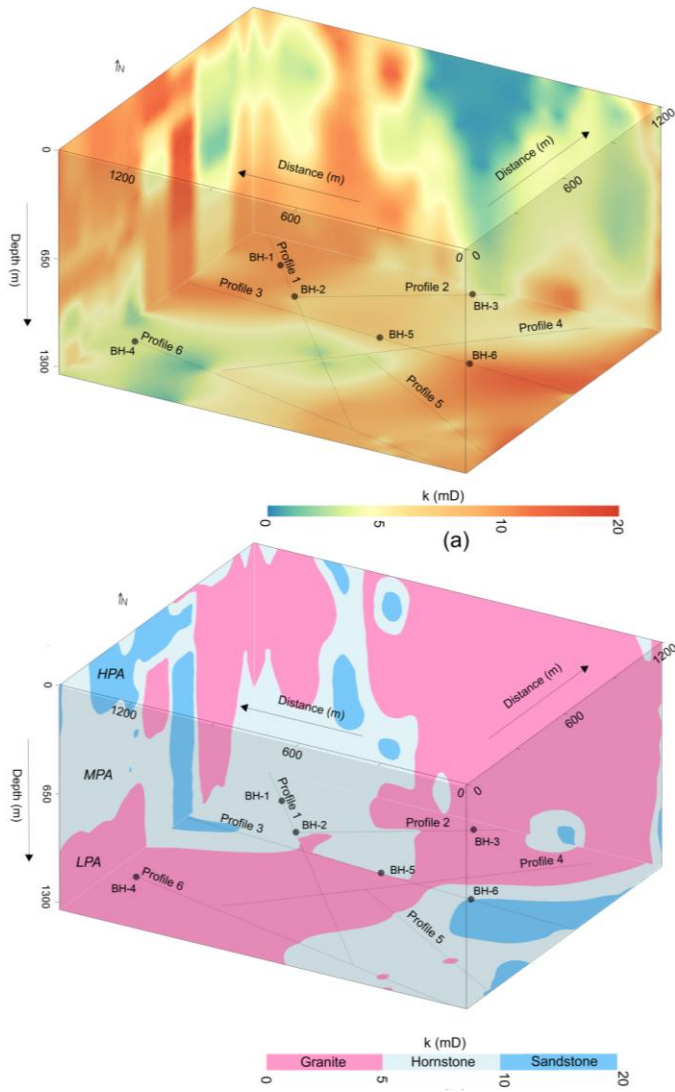
771 265–585 m, 605–845 m, and 1145–1315 m, line 4 at 90–390 m, 490–615 m, and 745–1115 m,
772 line 5 at 0–815 m, and surveyed line 6 at 1045–1345 m. A medium potential aquifer within
773 hornstone was identified along profile 1 at distances of 0–95 m, 190–260 m, 295–415 m, and
774 1185–1425 m; along profile 3 at 40–105 m, 215–275 m, 580–605 m, 850–910 m, 1010–1155 m,
775 and 1310–1410 m; along profile 4 at 45–90 m, 390–490 m, 590–685 m, and 1115–1185 m; and
776 along line 6 at 90–190 m, 215–275 m, 315–485 m, 505–605 m, and 635–1045 m. The sandstone
777 with significant aquifer potential was assessed across many locations: profile 1 at distances of
778 265–310 m, line 3 at 235–255 m and 915–1010 m, profile 4 within 0–45 m, and profile 6 at 0–90
779 m, 210–25 m, 275–305 m, 515–525 m, and 605–635 m. Fig. 10 indicates that elevated aquifer
780 yield is predominantly concentrated in the southern regions.



781

782 **Fig. 10.** The 3D k models, generated from the correlation of CSAMT and borehole data (with k
 783 represented on a color scale ranging from green to red), correspond to three groundwater potential
 784 aquifers: low potential aquifer (LPA), medium potential aquifer (MPA), and high potential aquifer (HPA),
 785 associated with three geological strata: granite, hornstone, and sandstone, respectively, for (a) the external
 786 view of the 3D k model, and (b) the analysis of the 3D k model from an external perspective

787 Fig. 11 (a, b) presents a comprehensive evaluation of the aquifer potential of the rock
788 mass for groundwater assessment, using a 3D internal perspective. At a subterranean depth of
789 1300 m, the low aquifer yield of granite was assessed using profile 1 across a distance of 515–
790 1215 m, profile 2 across 0–290 m, profile 3 across 390–690 m, profile 4 across 0–1145 m,
791 profile 5 across 0–195 m and 565–595 m, and profile 6 across lengths of 0–690 m and 1075–
792 1115 m. Hornstone associated to a medium potential aquifer was identified by profile 1 at
793 intervals of 0–540 m and 1215–1445 m, surveyed line 2 at 295–675 m, surveyed line 3 at 175–
794 395 m, 445–815 m, and 915–1035 m, profile 5 at 205–565 m and 610–815 m, and surveyed line
795 6 at 685–1080 m and 1110–1355 m. An aquifer with high potential, situated within sandstone,
796 was evaluated along profile 3 at intervals of 0–205 m and 1010–1400 m, as well as along line 5
797 at 810–815 m. Medium to high potential aquifers, located at a depth of 1300 m, are
798 predominantly found in the southeastern and northwestern regions, whilst the central areas are
799 primarily characterized by low potential aquifers. Fig. 11 illustrates the results of the 3D K
800 analysis, indicating that the northeastern and southwestern regions are primarily composed of
801 granite with negligible aquifer yield. The water retention capacity of the rock mass is enhanced
802 when observed from an aerial perspective. This enables a precise assessment of the aquifer
803 potential of geological strata for thorough groundwater analysis via 3D k modeling.



804

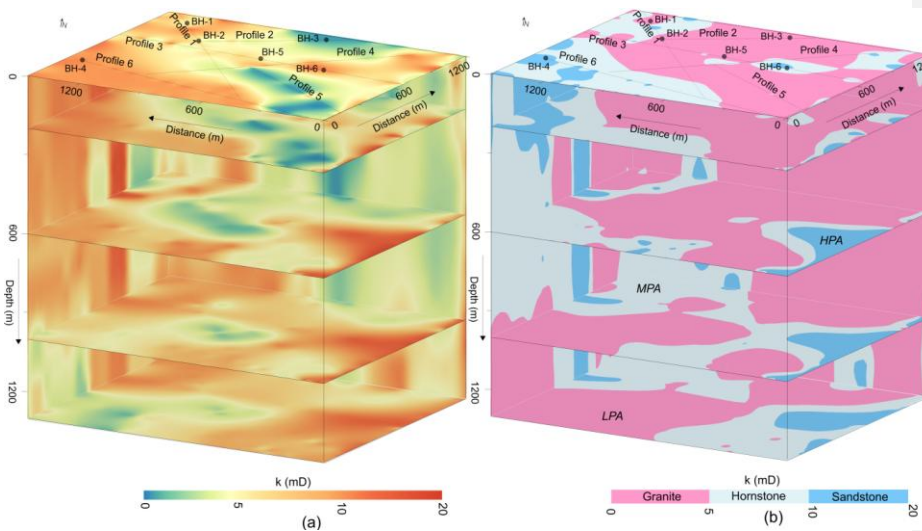
805 **Fig. 11.** The 3D k models, obtained from the correlation of CSAMT and borehole data (with k
 806 represented on a color scale ranging from green to red), illustrate three groundwater potential aquifers:
 807 low potential aquifer (LPA), medium potential aquifer (MPA), and high potential aquifer (HPA),

808 associated with three geological strata: granite, hornstone, and sandstone , respectively, for (a) the internal
809 view of the 3D k model, and (b) the analysis of the 3D (internal perspective) k model

810 **3.4 Depth-wise groundwater assessments**

811 Because of the scarcity of borehole data, it is not possible to use the observed k (borehole-based
812 k) to determine the water-bearing capacity of rock masses located below 200 m deep. The
813 evaluation of hard rock groundwater resources was made efficient, precise, and comprehensive
814 by creating a high link between drilling and CSAMT data. Because of this, k could be quickly
815 and accurately determined up to depths of 1300 m. From 2D/3D groundwater yield insights, we
816 were able to derive anticipated k values at 0, 200, 600, 1000, and 1300 m depths (Fig. 12).
817 Evaluation of groundwater at a depth of 1300 m was based on the following criteria: The
818 southwest and northeastern regions are assessed for granite, which constitutes over 45% of the
819 subsoil in low potential aquifer locations. Near the granite formation in the northwest and
820 southeast, we looked into hornstone, which comprised 40% of the medium potential aquifer. In
821 the eastern region, subsurface assessments were conducted on high-yield sandstone for over 15%
822 of the total. For groundwater evaluation at a depth of 1000 m, the following standards were
823 applied to understand the subsurface: The subsoil around the high potential aquifers in the
824 southeast consisted of 14% sandstone. Near the granite in the southeast and northwest areas, 38%
825 of the hornstone belonged to a medium potential aquifer. There were three boundaries, in the
826 middle, to the northeast, and to the southwest, in the subsurface, which was 52% granite and had
827 a poor aquifer yield. We examined the hydrogeological conditions at 600 m below ground using
828 the following criteria: in the central and northern areas, a low-yielding granite aquifer constituted
829 55% of the subsurface; hornstone in the west part was more common, accounting for 32% of the
830 subsurface and indicating a medium-yielding aquifer; and in the southeastern regions, sandstone

831 was the most studied, constituting 13% of the subsoil and indicating a high-yielding aquifer. To
 832 assess the hydrogeological conditions at a depth of 200 m, the following criteria were used:
 833 Granite with a low potential aquifer constituted 64% of the total in the center and northern parts.
 834 Hornstone with a medium yield aquifer comprised 26% of the underground in the southern
 835 regions. Research in the west focused on sandstone that made up 10% of the subsoil and had a
 836 high potential aquifer. Surface measurements taken at a depth of 0 m allowed us to determine the
 837 following hydrogeological conditions: While a medium potential aquifer is contained within 22%
 838 of the southwesterly surface's hornstone, and granite with 69% of the subsurface in the middle
 839 part. The sandstone, which is primarily located in the southwest, contains a high potential aquifer
 840 and is studied on 9% of the surface. Fig. 12 shows that as we descend then thickness of the
 841 granite from low yield aquifers decreases. Midway through, when depth drops to 600 to 700 m,
 842 groundwater conditions are at their worst. In the northwest, southeast, and southwest areas, there
 843 are rock masses that could represent aquifers, especially at depths lower than 700 m.



844

845 **Fig. 12.** (a) Geophysical permeability (k) imaging at depths of 0, 200, 600, 1000, and 1300 m, with k
846 values represented on a color scale ranging from green to red. (b) Evaluation of CSAMT-derived k values
847 (based on defined k ranges) at various depths for different aquifer types: low potential aquifer (LPA) in
848 granite, medium potential aquifer (MPA) in hornstone, and high potential aquifer (HPA) in sandstone

849 **3.5 Validation of predicted vs. measured permeability**

850 Groundwater evaluations across the study area benefit significantly from the precise and
851 systematic estimation of water-bearing capacity derived from CSAMT-based permeability (k).
852 As shown in Fig. 6–12, granite dominates the central, northeastern, and southwestern zones,
853 while hornstone, commonly classified as a type of metamorphosed sandstone, appears
854 predominantly in the southeastern, western, and northwestern regions. Sandstone is extensively
855 characterized in the eastern zones, with more limited data coverage in the west. Accurate
856 assessment of groundwater potential using only borehole data is challenging due to
857 inconsistencies in subsurface geological mapping. While drilling-based k values align with
858 CSAMT-predicted k at select points around 200 m depth near boreholes, spatial extrapolation
859 remains uncertain across larger areas. This mismatch underscores the difficulty of reliably
860 assessing aquifer properties based solely on sparse drilling, especially in complex lithological
861 settings.

862 ~~Table 2 presents the percentage of matching for the selected metrics, ascertained by~~
863 ~~juxtaposing the drill k with the CSAMT k. We compared the predicted k with the borehole-~~
864 ~~based k for several selected data points and observed the following % agreement: Upon~~
865 ~~experimentally connecting the first well, W1, to the fifth sounding along surveyed line 1 (P1-5),~~
866 ~~the percentage match at depths of 25 m and 115 m is 85% and 88%, respectively, as per Eq. (1).~~

867 ~~Following the application of Eq. (1), the percentage matching for sounding 9 along profile 1 (P1-~~
868 ~~9) and well number two (W2) at a depth of 10 meters and 130 meters, respectively, is 90% and~~
869 ~~100%. The percentage matching is 70 and 50, respectively, when W3 (well number three) and~~
870 ~~P2-3 (third sounding on line 2), which have depths of 85 and 150 meters, are merged, as per Eq.~~
871 ~~(1). We obtain %matching values of 82 and 85, respectively, with depths of 10 and 45 meters, by~~
872 ~~plugging the data from W4 (the fourth well) and P6-1 (the first sounding at line 6) using Eq. (1).~~
873 ~~We may acquire %matching of 84 and 85 for depths of 60 and 200 m, respectively, by~~
874 ~~integrating W5, the fifth well, and P3-15, the fifteenth sounding at line 3, using Eq. (1).~~
875 ~~Additionally, at a depth of 80 and 120 meters, the integration of W6 (well number six) and P3-21~~
876 ~~(the 21st sounding on line 3) using Eq. (1) results in a percentage matching of 95 and 85,~~
877 ~~respectively. The aforementioned comparison between the obtained and projected k indicates a~~
878 ~~lower degree of inaccuracy or strong matching. The comparison also demonstrates that predicted~~
879 ~~and measured k values generally fall into the same aquifer potential zone, even for data points~~
880 ~~with low %matching~~Table 2 summarizes the percentage agreement between measured (drill-
881 based) and predicted (CSAMT-based) k values. Agreement was evaluated by comparing
882 matched depth intervals for each borehole-sounding pair using Eq. (4). For instance: BH-1
883 paired with P1-5 shows matching percentages of 73%, 63%, and 100% at depths of 10 m, 40 m,
884 and 170 m, respectively. BH-2 and P1-9 exhibit matches of 80%, 77%, and 85% at 20 m, 60 m,
885 and 185 m depths. BH-3 with P2-3 yields lower agreement: 67%, 40%, and 30% at 10 m, 85 m,
886 and 200 m depths. BH-4 and P6-1 show strong correspondence with 70%, 86%, and 78% at 15
887 m, 100 m, and 180 m depths. BH-5 and P3-15 demonstrate high agreement of 80%, 94%, and
888 85% at 30 m, 135 m, and 200 m depths. BH-6 and P3-21 produce matches of 61%, 74%, and
889 71% at 45 m, 165 m, and 180 m depths, respectively.

890 These results reveal a generally high degree of consistency between observed and
 891 predicted k values, with discrepancies likely arising from local heterogeneities or measurement
 892 uncertainties. Notably, even when the %match is low, the k values from both methods tend to
 893 classify the location into the same aquifer potential zone (low, medium, or high), reinforcing the
 894 reliability of the CSAMT-based approach for broader regional assessments.

895 **Table 2**

896 Percentage match and deviation between drilling-derived permeability (k) and CSAMT-derived
 897 permeability (k') for 18 selected data points out of the total 116

<u>CSAMT data points (selected)</u>			<u>Drilling data</u>		<u>%Matching</u>	<u>Difference</u>	
<u>CSAMT</u>	<u>Resistivity</u>	<u>Predicted k'</u>	<u>Borehole</u>	<u>Depth</u>	<u>Measured</u>	<u>k' vs k</u>	<u>between</u>
<u>sounding</u>	<u>(Ωm)</u>	<u>using Eq.</u>	<u>name</u>	<u>(m)</u>	<u>k</u>		<u>k' and k</u>
<u>number</u>		<u>(4)</u>					
<u>P1-5</u>	<u>392</u>	<u>7.0</u>	<u>BH-1</u>	<u>10</u>	<u>9.6</u>	<u>73</u>	<u>2.6</u>
<u>P1-5</u>	<u>515</u>	<u>5.5</u>	<u>BH-1</u>	<u>40</u>	<u>8.7</u>	<u>63</u>	<u>3.2</u>
<u>P1-5</u>	<u>1080</u>	<u>1.8</u>	<u>BH-1</u>	<u>170</u>	<u>1.8</u>	<u>100</u>	<u>0.0</u>
<u>P1-9</u>	<u>669</u>	<u>4.0</u>	<u>BH-2</u>	<u>20</u>	<u>5.0</u>	<u>80</u>	<u>1.0</u>
<u>P1-9</u>	<u>863</u>	<u>2.7</u>	<u>BH-2</u>	<u>60</u>	<u>3.5</u>	<u>77</u>	<u>0.8</u>
<u>P1-9</u>	<u>1354</u>	<u>1.02</u>	<u>BH-2</u>	<u>185</u>	<u>1.2</u>	<u>85</u>	<u>0.18</u>
<u>P2-3</u>	<u>2187</u>	<u>0.2</u>	<u>BH-3</u>	<u>10</u>	<u>0.3</u>	<u>67</u>	<u>0.1</u>
<u>P2-3</u>	<u>2988</u>	<u>0.04</u>	<u>BH-3</u>	<u>85</u>	<u>0.1</u>	<u>40</u>	<u>0.06</u>
<u>P2-3</u>	<u>4765</u>	<u>0.003</u>	<u>BH-3</u>	<u>200</u>	<u>0.01</u>	<u>30</u>	<u>0.007</u>
<u>P6-1</u>	<u>50</u>	<u>13.9</u>	<u>BH-4</u>	<u>15</u>	<u>19.9</u>	<u>70</u>	<u>6.0</u>
<u>P6-1</u>	<u>200</u>	<u>10.3</u>	<u>BH-4</u>	<u>100</u>	<u>12.0</u>	<u>86</u>	<u>1.7</u>
<u>P6-1</u>	<u>348</u>	<u>7.7</u>	<u>BH-4</u>	<u>180</u>	<u>9.9</u>	<u>78</u>	<u>2.2</u>

<u>P3-15</u>	<u>792</u>	<u>3.3</u>	<u>BH-5</u>	<u>30</u>	<u>4.1</u>	<u>80</u>	<u>0.8</u>
<u>P3-15</u>	<u>1157</u>	<u>1.5</u>	<u>BH-5</u>	<u>135</u>	<u>1.6</u>	<u>94</u>	<u>0.1</u>
<u>P3-15</u>	<u>1412</u>	<u>0.91</u>	<u>BH-5</u>	<u>200</u>	<u>1.07</u>	<u>85</u>	<u>0.16</u>
<u>P3-21</u>	<u>165</u>	<u>11.1</u>	<u>BH-6</u>	<u>45</u>	<u>18.2</u>	<u>61</u>	<u>7.1</u>
<u>P3-21</u>	<u>708</u>	<u>3.7</u>	<u>BH-6</u>	<u>165</u>	<u>5.0</u>	<u>74</u>	<u>1.3</u>
<u>P3-21</u>	<u>846</u>	<u>2.8</u>	<u>BH-6</u>	<u>180</u>	<u>2.0</u>	<u>71</u>	<u>0.8</u>

898

Formatted: Centered

899 **4 Discussions**

900 ~~Groundwater research is seeing a rise in the use of geophysical technology. Groundwater~~
901 ~~evaluations have shown promise in prior studies when geophysical and drilling data are~~
902 ~~combined. We can determine a rock mass's water-bearing potential by looking at its hydraulic~~
903 ~~properties. Drilling boreholes to measure permeability (k) is the best and most feasible way to~~
904 ~~measure hydraulic parameters for groundwater evaluations. Through the use of geophysical~~
905 ~~methods, this study is the first to indirectly obtain 2D/3D k at depths more than 1 km in a context~~
906 ~~with a diverse range of rocks.~~

907 ~~This work introduces CSAMT, a novel geophysical method for assessing the water-~~
908 ~~bearing capacity of rock masses, which allows for more precise groundwater evaluation even~~
909 ~~when sufficient borehole data is unavailable. This paves the way for a comprehensive assessment~~
910 ~~of hard rock groundwater at depths above 1 kilometer by means of the anticipated hydraulic~~
911 ~~parameter k. In light of the varied terrain in southern China, our approach provides a versatile~~
912 ~~empirical correlation based on the region's massive geophysical dataset and limited drill data.~~
913 ~~The lithologies and rocks were categorized using the same set of k values as were utilized in the~~
914 ~~aquifer models. The rocks are classified into three groups based on different aquifer potential~~

915 ~~zones: fresh granite zone of low potential aquifer (LPA), sandstone zone of high potential aquifer~~
916 ~~(HPA), and hornstone zone of medium potential aquifer (MPA), which lies in the middle zone~~
917 ~~between the two possible aquifers. The calculations can be used to find the overall water bearing~~
918 ~~capacity of the rock formation in these particular geological settings since they are based on~~
919 ~~resistivity k measurements of hornstone, granite, and sandstone. The precise parameter ranges~~
920 ~~are defined by taking into account the local environment and the rock's composition. The precise~~
921 ~~rock mass class of a possible aquifer can be determined using the well established flexible~~
922 ~~equations, taking into account the hydrogeological conditions of the location. Any geological~~
923 ~~context can benefit from the generalized equations that can be derived using the suggested~~
924 ~~method. Because it is relative, a rock unit's k resistivity range could change depending on are to~~
925 ~~area. Drilling five or more boreholes across the entire area, with at least five measurements~~
926 ~~collected from the rock unit in each, usually yields a reliable empirical equation. The reliability~~
927 ~~of the empirical equation is greatly affected by the ranges of k resistivity and the quantity of~~
928 ~~geophysical borehole datasets. A more precise calculation of k is possible with the use of more~~
929 ~~datasets in correlation analysis. In the study area, a total of 116 k resistivity data sets were used~~
930 ~~from six boreholes, these data sets cover all three lithologies with resistivity range 35-4765 and k~~
931 ~~range 0.001-19.9 mD. The 116 data sets cover the entire resistivity k range (i.e., resistivity and k~~
932 ~~range over entire area is 30-4800 and 0.001-20 mD) with almost equally spaced of the resistivity-~~
933 ~~k values. With real and estimated k matching rates over 80%, most datasets showed an~~
934 ~~outstanding level of accuracy (Table 2). The established equation provides a poor fit between the~~
935 ~~anticipated and actual k, especially for very high resistivity and low k values. For instance, the~~
936 ~~anticipated and calculated k values are in the same LPA zone, even though there was only a 70%~~
937 ~~and 50% match between W3 and P2-3 at 85 and 150 meters of depth, respectively. All~~

938 lithologies and rock types, including granite, hornstone, and sandstone, are represented in the
939 resistivity k ranges used for correlation analysis across the project territory. In order to get
940 trustworthy results, the researchers may have used the drill locations as a proxy for the rock unit
941 characteristics of the whole study site. It may be more accurate to use distinct formulae for each
942 kind of rock unit to find k rather than using a single formula to evaluate several geological layers.
943 While there is sufficient drilling data for each rock mass unit, separate equations may be more
944 effective. Since this correlation is the basis for the expected k , the locations of the surveyed lines
945 are crucial to its correct calculation. As a result, regions near geophysical profiles yield
946 somewhat more accurate findings from two and three dimensional k models than regions far
947 from these profiles. We can estimate k in similar geological conditions using the resultant
948 equation when drilling data is not available.

949 CSAMT is heavily utilized for reducing the effect of weak natural signals and for exploring
950 subterranean structures. However, there are a number of factors that might influence resistivity
951 measurements, including transmission devices, electrical lines, metal obstructions, etc., and this
952 can cause results and interpretations to be unclear. Good CSAMT survey design, however,
953 mitigates these effects and yields accurate results, as demonstrated in this study. Data of a high
954 quality could be collected since the project site was free of electrical and human interference.
955 With a resistivity of 28 Ωm and a k value of 20 m/d, the sandstone rock mass was found to have
956 the highest water holding capacity. However, the rock mass (granite) was found to have a
957 minimal water bearing capability of 0.01 m/d when the resistivity value was tested at 5000 Ωm .
958 When comparing the geophysical k to the drilling k , the latter provides a more precise and
959 comprehensive evaluation of the rock mass's water-bearing capacity while the former decreases
960 the variability in the anticipated hydrogeological model. Due to a lack of boring trials,

961 ~~hydrogeological models used to evaluate groundwater in highly heterogeneous hard rock are thus~~
962 ~~profoundly flawed. When hydrogeological models are accurate but borehole data is insufficient,~~
963 ~~geophysical approaches can help fill the gap.~~The integration of geophysical methods into
964 groundwater research has gained significant traction in recent years, offering scalable and cost-
965 effective alternatives to traditional drilling. While borehole investigations remain the most direct
966 method for assessing permeability (k), they are often constrained by high costs, logistical
967 complexity, and limited spatial coverage, particularly in deep, geologically heterogeneous
968 terrains. Our study presents a novel and reliable framework for indirect 2D and 3D permeability
969 modeling to depths exceeding 1 km, achieved by integrating CSAMT with borehole-derived data
970 in a lithologically complex setting. This methodology addresses critical hydrogeological
971 challenges in our study area, where surface water resources are limited and shallow granite
972 exhibits low permeability. By contrast, deeper fractured granite, hornstone, and sandstone
973 formations demonstrate significantly greater groundwater potential. The resulting deep aquifer
974 characterizations are aligned with China's national water security initiatives and provide
975 valuable input for sustainable groundwater management in the context of increasing water stress
976 and climate variability. Building on this foundation, our previous research (Hasan and Shang,
977 2022; Hasan et al., 2025) applied similar geophysical strategies in geotechnical engineering,
978 where 2D and 3D modeling of Rock Quality Designation (RQD) and rock mass integrity
979 coefficient (Kv), two key geomechanical parameters, was conducted using empirical correlations
980 between borehole core data and resistivity derived from ERT/CSAMT. These methods were
981 instrumental in site evaluations for major national infrastructure projects, including the
982 Accelerator Driven System (ADS) in Huizhou and the Jiangmen Underground Neutrino
983 Observatory (JUNO), located approximately 700 m below ground in South Guangdong, adjacent

984 to the present study area. The successful deployment of this geophysical approach in both
985 hydrogeological and geotechnical domains underscores its reliability, scalability, and
986 interdisciplinary value for large-scale subsurface characterization.

987 CSAMT, introduced in the 1970s, remains uniquely valuable for deep subsurface
988 exploration, particularly in resistive, hard rock environments. Unlike conventional geophysical
989 techniques, CSAMT excels at delineating lithological boundaries and fluid-bearing zones.
990 Recent advances in instrumentation and inversion techniques have significantly enhanced its
991 resolution and depth penetration, enabling applications such as ours that extend its use beyond
992 historical limits. The novelty of this study lies not in the use of CSAMT or resistivity–
993 permeability relationships themselves, both of which are well-established, but in their integrated,
994 site-specific application to a geologically complex and deeply fractured hard rock environment
995 This is the first study to successfully model permeability at depths of up to 1300 m in granite,
996 sandstone, and hornstone using a data-driven approach validated by high-resolution borehole
997 data.

998 In this study, we established an empirical relationship between resistivity and
999 permeability using 116 co-located data pairs across the three dominant lithologies in the study
1000 area: 62 for granite, 31 for sandstone, and 23 for hornstone. The dataset spans a resistivity range
1001 of 35 to 4,765 Ωm and a permeability range of 0.01 to 19.9 mD, and is evenly distributed across
1002 the geological formations, thereby minimizing lithological bias and ensuring robust calibration.
1003 The derived correlation yielded a high coefficient of determination ($R^2 = 0.96$), indicating strong
1004 predictive capability. The lithological classification emerging from this resistivity–permeability
1005 relationship is both geologically consistent and empirically validated by field observations and

1006 borehole data: low-permeability granite (>700 Ωm ; k = 0–5 mD), moderate-permeability
1007 hornstone (350–700 Ωm ; k = 5–10 mD), and high-permeability sandstone (<350 Ωm ; k = 10–
1008 20 mD). These ranges reflect the distinct hydrogeological behavior of each unit under site-
1009 specific geological conditions. We emphasize, however, that these resistivity–k associations are
1010 localized and must be recalibrated for application in other regions with different geological
1011 settings. The strength of our approach lies in its ability to significantly reduce the reliance on
1012 extensive borehole drilling and direct permeability measurements, which are both cost-
1013 prohibitive and operationally challenging, particularly in deep or structurally complex terrains.
1014 By using a limited number of boreholes for calibration, our method enables the construction of
1015 high-resolution 2D and 3D permeability models over large areas using CSAMT-derived
1016 resistivity. If extensive borehole data were readily available or required, the added value of our
1017 geophysical integration would diminish, along with its cost-effectiveness and broader
1018 applicability. Thus, the novelty and practical relevance of our approach stem from its ability to
1019 enhance subsurface characterization in data-scarce environments while minimizing invasive
1020 testing.

1021 The fitted relationship between resistivity and permeability (k) in our study (shown in
1022 Fig. 5) is inherently influenced by several factors, including the geological setting, lithological
1023 variability, data distribution, and the accuracy of both resistivity and permeability measurements.
1024 The broad dynamic range observed in our dataset, resistivity values from 35 to 4,765 Ωm and
1025 permeability values from 0.01 to 19.9 mD, provides a solid foundation for resolving trends
1026 across all three dominant lithologies: sandstone, granite, and hornstone. This wide spread is
1027 particularly beneficial for characterizing high-resistivity rocks such as granite, where
1028 permeability remains consistently low and varies only slightly. In such cases, even large

1029 differences in resistivity correspond to minor changes in k, resulting in a smoother inverse trend.
1030 Conversely, in the lower resistivity range (e.g., <1500 Ω m) where permeability exceeds 1 mD,
1031 small changes in resistivity correspond to larger variations in k, resulting in a more scattered and
1032 nonlinear trend in the correlation. This behavior is expected and reflects real geological
1033 variability.

1034 To ensure accuracy and reduce uncertainty, we implemented a robust workflow across all
1035 stages of data acquisition, processing, inversion, and modeling. For CSAMT, we employed
1036 careful survey design, optimized electrode configurations, and applied advanced filtering and
1037 static shift corrections. Inversion incorporated multidimensional modeling with borehole-
1038 constrained a priori information to improve resolution and reduce non-uniqueness. The
1039 permeability data from borehole cores were collected under controlled conditions, using high-
1040 quality, undisturbed samples from six boreholes, thereby reducing lab-to-field scale
1041 discrepancies. These efforts, combined with integrated lithological data, yielded a reliable
1042 permeability model capable of informing groundwater assessments across the study domain.

1043 Matching between measured and predicted permeability (k vs. k') was also rigorously
1044 validated (Table 2). Among 18 selected points from boreholes, 10 showed a difference of less
1045 than 1 mD, with only two exceeding 4 mD. Despite minor deviations, all points were accurately
1046 classified by lithology. This confirms the empirical model's reliability and its utility for regional-
1047 scale k prediction, even in areas lacking direct measurements. The geophysical model effectively
1048 compensates for sparse drilling data, offering a scalable and cost-effective tool for
1049 hydrogeological evaluation in hard rock terrains.

1050 While pumping tests provide average hydraulic conductivity over large volumes of
1051 subsurface material, making them suitable for establishing 1D correlation with spatially averaged
1052 geophysical data, they are less appropriate for high-resolution 2D or 3D modeling. In contrast,
1053 our objective was to develop detailed 2D and 3D permeability models that reflect the spatial
1054 heterogeneity of the subsurface. Achieving this level of resolution requires point-specific
1055 permeability measurements at varying depths, which align more precisely with the localized
1056 nature of resistivity values derived from CSAMT data. To meet this requirement, we employed
1057 rock core analysis rather than traditional pumping tests. Rock core testing offers the advantage of
1058 extracting permeability data at discrete depths and locations, providing a direct and fine-scale
1059 match with CSAMT-derived resistivity. This approach enhances the accuracy of the resistivity–
1060 permeability relationship and allows for more reliable permeability modeling in complex
1061 geological settings. Scale compatibility between CSAMT-derived resistivity and borehole-
1062 derived permeability (k) values was carefully addressed. The typical lateral resolution of
1063 CSAMT (~50 × 50 meters) closely matches the spatial scale of the core-based permeability data
1064 used in this study.

1065 Furthermore, our findings were cross-validated against existing geological data from both
1066 local and national surveys, revealing strong alignment with the established stratigraphy and
1067 hydrogeological characteristics of the region. This consistency reinforces the validity of our
1068 integrated geophysical–borehole approach, which offers a scientifically robust and practically
1069 scalable framework for estimating permeability in structurally complex and data-scarce terrains.
1070 While the methodology is rooted in established geophysical principles, the innovation of this
1071 study lies in its comprehensive, site-specific implementation, combining deep permeability
1072 modeling, field-based verification, and empirical calibration specifically tailored to the local

1073 geological context. Overall, the results underscore the considerable potential of geophysical
1074 techniques, particularly CSAMT, in supporting sustainable groundwater exploration and
1075 management at significant depths-

1076 **5 Conclusions**

1077 This study presents an innovative, non-invasive approach to deep groundwater exploration using
1078 controlled-source audio-frequency magnetotellurics (CSAMT). For the first time, CSAMT has
1079 been applied to indirectly estimate two and three dimensional permeability (k) distributions in
1080 geologically complex hard rock terrains, extending to depths of up to 1300 m. While borehole
1081 drilling remains the conventional method for evaluating hydraulic parameters, it is often costly,
1082 logistically challenging, and limited in spatial coverage. Our approach significantly reduces
1083 reliance on boreholes while providing a more detailed and spatially extensive hydrogeological
1084 assessment. Using co-located CSAMT and borehole data, we developed a robust empirical
1085 equation to estimate permeability based on resistivity values. This equation was applied across
1086 the study area to generate high-resolution k models that align closely with the known geology
1087 and stratigraphy. Specifically, sandstone, classified as a high potential aquifer (HPA), exhibited
1088 resistivity below 350 Ωm and permeability ranging from 10–20 mD. Hornstone, as a medium
1089 potential aquifer (MPA), showed resistivity between 350–700 Ωm and k values of 5–10 mD.
1090 Granite, representing a low potential aquifer (LPA), had resistivity above 700 Ωm with k ranging
1091 from 0–5 mD. These trends confirm the expected relationship between lower resistivity and
1092 higher permeability, validating the physical basis of our model.

1093 Our 2D/3D permeability models further revealed that the most promising zones for deep
1094 groundwater occur in central regions below 700 m and around granite formations down to 1300

1095 m. The close alignment between the modeled permeability and regional hydrogeological features
1096 highlights the reliability and predictive power of this method. By bridging the gap between
1097 sparse borehole data and robust hydrogeological models, CSAMT offers a cost-effective and
1098 scalable alternative for evaluating groundwater potential in hard rock regions. Looking forward,
1099 future research could enhance this method by refining the empirical models using broader
1100 hydrogeological datasets and integrating other geophysical parameters. This would deepen our
1101 understanding of the relationship between aquifer properties and geophysical signals, ultimately
1102 improving the reliability of groundwater assessments in challenging geological settings.

1103 **Code availability**

1104 Software application or custom code supports the published claims and complies with field
1105 standards

1106 **Data availability**

1107 Data available on request from the corresponding author

1108 **Author contributions**

1109 MH conceptualized the research goals and developed the methodology. MH and LS found the
1110 funding for the project. MH developed the code and prepared its visualization, and LS provided
1111 programming support and analysis tools. MH prepared the original draft.

1112 **Declaration of competing interest**

1113 The authors declare that they have no conflict of interest.

1114 **Acknowledgements**

1115 The authors wish to acknowledge the institutions that facilitated the research for this study: the
1116 State Key Laboratory of Mountain Hazards and Engineering Resilience, Institute of Mountain
1117 Hazards and Environment, Chinese Academy of Sciences, and China-Pakistan Joint Research
1118 Center on Earth Sciences, CAS-HEC, Islamabad, Pakistan.

1119 **Financial support**

1120 This research was financially supported by the National Natural Science Foundation of China's
1121 Research Fund for International Young Scientists (RFIS-I) (Grant No. 42350410442), and
1122 International Science and Technology Cooperation Program of Shanghai Cooperation
1123 Organization, Science and Technology Department, Xinjiang, China (Grant No. E202301005).

1124 **References**

- 1125 1. Abbas, M., Deparis, J., Isch, A., Mallet, C., Jodry, C., Azaroual, M., Abbar, B., and
1126 Baltassat, J.M.: Hydrogeophysical characterization and determination of petrophysical
1127 parameters by integrating geophysical and hydrogeological data at the limestone vadose
1128 zone of the Beauce aquifer, *Journal of Hydrology*, 615, 128725, 2022.
- 1129 2. Allègre, V., Brodsky, E.E., Xue, L., Nale, S.M., Parker, B.L., and Cherry, J.A.: Using
1130 earth-tide induced water pressure changes to measure in situ permeability: A comparison
1131 with long-term pumping tests, *Water Resour. Res.*, 52, 3113–3126, 2016.
- 1132 3. Amiotte Suchet, P., Probst, J.L., and Ludwig, W.: Worldwide distribution of continental
1133 rock lithology: Implications for the atmospheric/ soil CO₂ uptake by continental
1134 weathering and alkalinity river transport to the oceans, *Glob Biogeochem Cycles*, 17,
1135 1038, 2003.

1136 4. An, Z., and Di, Q.: Investigation of geological structures with a view to HLRW disposal,
1137 as revealed through 3D inversion of aeromagnetic and gravity data and the results of
1138 CSAMT exploration, *Journal of Applied Geophysics*, 135, 204–211, 2016.

Formatted: Pattern: Clear

1139 4.5. Archie, G.E.: The electrical resistivity log as an aid in determining some reservoir
1140 characteristics, Transactions of the AIME, 146(1), 54–62, 1942.

Formatted: Font: (Default) Times New Roman, 12 pt, Not Bold

Formatted: Font: (Default) Times New Roman, 12 pt, Not Bold

1141 6. Asfahani, J.: Estimation of the hydraulic parameters by using an alternative vertical
1142 electrical sounding technique: case study from semiarid Khanasser valley region
1143 Northern Syria, *Acta Geophys*, 71, 997–1013, 2023.

Formatted: Font: (Default) Times New Roman, 12 pt, Not Bold

Formatted: Font: (Default) Times New Roman, 12 pt, Not Bold

1144 5-7. ASTM.: Standard Test Methods for Measurement of Hydraulic Conductivity of Saturated
1145 Porous Materials Using a Flexible Wall Permeameter (ASTM D5084-21), ASTM
1146 International, 2021.

1147 8. Bai, D., Unsworth, M., Meju, M., Ma, X., Teng, J., Kong, X., Sun, Y., Sun, J., Wang, L.,
1148 Jiang, C., Zhao, C., Xiao, P., and Liu, M.: Crustal deformation of the eastern Tibetan
1149 plateau revealed by magnetotelluric imaging, *Nature Geosci.*, 3, 358–362, 2010.

Formatted: Pattern: Clear

1150 6-9. Bear, J.: Dynamics of Fluids in Porous Media, Elsevier, 1972.

Formatted: Font: (Default) Times New Roman, 12 pt, Not Bold

1151 10. Bentley, L.R., and Gharibi, M.: Two- and three-dimensional electrical resistivity imaging
1152 at a heterogeneous remediation site, *Geophysics*, 69, 674–680, 2004.

Formatted: Font: (Default) Times New Roman, 12 pt, Not Bold

1153 7-11. Binley, A., and Kemna, A.: DC resistivity and induced polarization methods, In
1154 Hydrogeophysics, Springer, pp. 129–156, 129 2005.

Formatted: Font: (Default) Times New Roman, 12 pt, Not Bold

Formatted: Font: (Default) Times New Roman, 12 pt, Not Bold

1155 12. Borah, U.K., and Patro, P.K.: Estimation of the depth of investigation in the
1156 magnetotelluric method from the phase, *Geophysics*, 84 (6), E377–E385, 2019.

Formatted: Font: (Default) Times New Roman, 12 pt, Not Bold

Formatted: Pattern: Clear

1157 8-13. Brace, W.F., Walsh, J.B., and Frangos, W.T.: Permeability of granite under high
1158 pressure, Journal of Geophysical Research, 73(6), 2225–2236, 1968.

1159 | ~~9-14.~~ Cagniard, L.: Basic theory of the magneto-telluric method of geophysical
1160 | prospecting, *Geophysics*, 18 (3), 605–635, 1953.

1161 | ~~10-15.~~ Camporese, M., Cassiani, G., Deiana, R., and Salandin, P.: Assessment of local
1162 | hydraulic properties from electrical resistivity tomography monitoring of a
1163 | three-dimensional synthetic tracer test experiment, *Water Resources Research*, 47 (12),
1164 | 2011.

1165 | 16. Carbillet, L., Griffiths, L., Heap, M.J., Duwiquet, H., Baud, P., Violay, M.E.S., Reuschlé,
1166 | T., and Guillou-Frottier, L.: The Influence of Micro- and Macrocracks on the
1167 | Permeability of Granite, *Rock Mech Rock Eng*, [https://doi.org/10.1007/s00603-024-](https://doi.org/10.1007/s00603-024-04174-0)
1168 | [04174-0](https://doi.org/10.1007/s00603-024-04174-0), 2024.

1169 | 17. Carman, P.C.: Flow of Gases through Porous Media, Butterworths Scientific Publications,
1170 | 1956.

1171 | 18. Clennell, M.B.: Tortuosity: a guide through the maze, Geological Society, London,
1172 | Special Publications, 122(1), 299–344, 1997.

1173 | ~~11-19.~~ Courtois, N., Dewandel, B., Bhuvana, V., Ahmed, S., and Chandra, S.:
1174 | Contribution of vertical and horizontal fractures to the groundwater flow in crystalline
1175 | hard rock aquifers: Insights from a comparative study of three different sites in southern
1176 | India, *Hydrogeology Journal*, 18(8), 1811–1827, 2010.

1177 | ~~12-20.~~ De Lima, O.A.L., and Niwas, S.: Estimation of hydraulic parameters of shaly
1178 | sandstone aquifers from geological measurements, *J Hydrol*, 235, 12–26, 2000.

1179 | ~~13-21.~~ Dell'Oca, A., Guadagnini, A., and Riva, M.: Interpretation of multi-scale
1180 | permeability data through an information theory perspective, *Hydrol. Earth Syst. Sci.*, 24,
1181 | 3097–3109, 2020.

Formatted: Font: (Asian) Times New Roman

Formatted: Font: (Default) Times New Roman, 12 pt, Not Bold

Formatted: Font: (Default) Times New Roman, 12 pt, Not Bold

Formatted: Font: (Default) Times New Roman, 12 pt, Not Bold

Formatted: Font: (Asian) Times New Roman

Formatted: Font: (Default) Times New Roman, 12 pt, Not Bold

Formatted: Font: (Default) Times New Roman, 12 pt, Not Bold

Formatted: Font: (Default) Times New Roman, 12 pt, Not Bold

1182 ~~14-22.~~ Dewandel, B., Lachassagne, P., Wyns, R., Maréchal, J.C., and Krishnamurthy,
1183 N.S.: A generalized 3-D geological and hydrogeological conceptual model of granite
1184 aquifers controlled by single or multiphase weathering, Journal of Hydrology, 330(1–2),
1185 260–284, 2006.

1186 ~~15-23.~~ Di, Q., Fu, C., An, Z., Wang, R., Wang, G., Wang, M., Qi, S., and Liang, P.: An
1187 application of CSAMT for detecting weak geological structures near the deeply buried
1188 long tunnel of the Shijiazhuang-Taiyuan passenger railway line in the Taihang Mountains,
1189 Engineering Geology, 268, 105517, 2020.

1190 24. Esmacilpour, M., Ghanbarian, B., Sousa, R., Peter, R., and King, P.R.: Estimating
1191 Permeability and Its Scale Dependence at Pore Scale Using Renormalization Group
1192 Theory, Water Resources Research, 59 (5), e2022WR033462, 2023.

1193 25. Faybishenko, B., Witherspoon, P.A., and Benson, S.M.: Fracture-matrix interaction in
1194 unsaturated fractured rock: Experimental observations and modeling, Journal of
1195 Contaminant Hydrology, 46(3–4), 223–256, 2000.

1196 ~~16-26.~~ Ferguson, G., McIntosh, J.C., Jasechko, S., Kim, J.H., Famiglietti, J.S., and
1197 McDonnell, J.J.: Groundwater deeper than 500 m contributes less than 0.1% of global
1198 river discharge, Communication Earth and Environment, 4, 48, 2023.

1199 ~~17-27.~~ Fernando, A., and Pacheco, L.: Regional groundwater flow in hard rocks, Science
1200 of the Total Environment, 506–507, 182–195, 2015.

1201 ~~18-28.~~ Fiandaca, G., Maurya, P.K., Balbarini, N., Hördt, A., Christiansen, A.V., Foged,
1202 N., Bjerg, P.L., and Auken, E.: Permeability estimation directly from logging-while-
1203 drilling induced polarization data, Water Resources Research, 54, 2851–2870, 2018.

Formatted: Font: (Asian) Times New Roman,
Pattern: Clear

Formatted: Font: (Asian) Times New Roman,
Pattern: Clear

1204 ~~19-29.~~ Fu, C., Di, Q., and An, Z.: Application of the CSAMT method to groundwater
1205 exploration in a metropolitan environment, *Geophysics*, 78 (5), 201–B209, 2013.

1206 ~~20-30.~~ Fusheng, G., Haiyan, Y., Zengqian, H., Zhichun, W., Ziyu, L., Guocan, W., Linfu,
1207 X., Ye, G., and Wanpeng, Z.: Structural setting of the Zoujiashan-Julong'an region,
1208 Xiangshan volcanic basin, China, interpreted from modern CSAMT data, *Ore Geology*
1209 *Reviews*, 150, 105180, 2022.

1210 31. Gerke, H.H., Dusek, J., and Vogel, T.: Mass transfer effects in 2-D dual-permeability
1211 modeling of field preferential bromide leaching with drain effluent, *Hydrol. Earth Syst.*
1212 *Sci. Discuss.*, 8, 5917–5967, 2011.

Formatted: Font: (Default) Times New Roman, 12 pt

1213 32. Gleeson, T., Moosdorf, N., Hartmann, J., and van Beek, L.P.H.: A glimpse beneath
1214 earth's surface: Global hydrogeology maps (GLHYMPS) of permeability and porosity,
1215 Geophysical Research Letters, 43(2), 1–8, 2016.

Formatted: Font: (Asian) +Body Asian

1216 33. Glover, P.W.J.: Geophysical properties of the near surface Earth: electrical properties,
1217 Treatise on Geophysics, 11, 89–137, 2015.

Formatted: Font: (Default) Times New Roman, 12 pt

Formatted: Font: (Default) Times New Roman, 12 pt

1218 ~~21-34.~~ Hasan, M., Su, L., Cui, P., and Shang, Y.: Development of deep-underground
1219 engineering structures via 2D and 3D ROD prediction using non-invasive
1220 CSAMT, *Scientific Reports*, 15, 1403, 2025.

Formatted: Font: (Default) Times New Roman, 12 pt

Formatted: Font: (Asian) +Body Asian

Formatted: Font: Not Italic

1221 ~~22-35.~~ Hasan, M., and Shang, Y.: Geophysical evaluation of geological model
1222 uncertainty for infrastructure design and groundwater assessments, *Engineering Geology*,
1223 299, 106560, 2022.

1224 36. Hasan, M., Shang, Y., Jin, W., and Akhter, G.: Estimation of hydraulic parameters in a
1225 hard rock aquifer using integrated surface geoelectrical method and pumping test data in
1226 southeast Guangdong China, *Geosci J*, 25 (2), 223–242, 2021.

1227 ~~23-37.~~ Hsieh, P.A., Neuzil, C.E., and Bredehoeft, J.D.: Flow tests in the crystalline rocks
1228 of the Whiteshell Research Area, Manitoba, Canada, Water Resources Research, 17(2),
1229 496–504, 1981.

1230 ~~24-38.~~ Hu, X.Y., Peng, R.H., Wu, G.J., Wang, W.P., Huo, G.P., and Han, B.: Mineral
1231 exploration using CSAMT data: application to Longmen region metallogenic belt,
1232 Guangdong Province, China, Geophysics, 78, B111–B119, 2013.

1233 39. Hubbard, S.H., and Rubin, Y.: Hydrogeological parameter estimation using geophysical
1234 data: a review of selected techniques, J Contam Hydrol, 45 (3), 34, 2002.

1235 ~~25-40.~~ ISRM.: Suggested methods for determining the permeability of rocks,
1236 International Society for Rock Mechanics, 2007.

1237 ~~26-41.~~ Jardani, A., Revil, A., Dupont, J. P., and Benderjitter, Y.: Detection of preferential
1238 groundwater pathways in sinkhole fields using self-potential methods, Journal of
1239 Hydrology, 335(1–2), 187–199, 2007.

1240 42. Jasechko, S., Seybold, H., Perrone, D., Fan, Y., Shamsudduha, M., Taylor, R.G., Fallatah,
1241 O., and Kirchner, J.W.: Rapid groundwater decline and some cases of recovery in
1242 aquifers globally, Nature, 625, 715–721, 2024.

1243 ~~27-43.~~ Jiang, Y., Wu, X., and Shi, Z.: A novel model to estimate permeability from
1244 formation resistivity, Journal of Petroleum Science and Engineering, 124, 15–23, 2014.

1245 ~~28-44.~~ Kouadio, K.L., Liu, R., Malory, A.O., and Liu, C.: A novel approach for water
1246 reservoir mapping using controlled source audio-frequency magnetotelluric in Xingning
1247 area, Hunan Province, China, Geophysical Prospecting, 71, 1708–1727, 2023.

Formatted: Font: (Default) Times New Roman, 12 pt

Formatted: Pattern: Clear

Formatted: Font: (Default) Times New Roman, 12 pt

Formatted: Font: (Default) Times New Roman, 12 pt

Formatted: Font: (Default) Times New Roman, 12 pt

1248 ~~29-45.~~ [Lachassagne, P., Wyns, R., and Dewandel, B.: The fracture permeability in hard](#)
1249 [rocks aquifers and its dynamic modeling: An integrated conceptual model of weathered](#)
1250 [crystalline aquifers, Hydrogeology Journal, 29\(1\), 1–20, 2021.](#)

1251 ~~30-46.~~ [Laghari, A.N., Vanham, D., and Rauch, W.: The Indus basin in the framework of](#)
1252 [current and future water resources management, Hydrology and Earth System](#)
1253 [Sciences, 16 \(4\), 1063–1083, 2012.](#)

1254 [47.](#) [Lin, C.H., Lin, C.P., Hung, Y.C., Chung, C.C., Wu, P.L., and Liu, H.C.: Application of](#)
1255 [geophysical methods in a dam project: Life cycle perspective and Taiwan experience,](#)
1256 [Journal of Applied Geophysics, 158, 82–92, 2018.](#)

1257 ~~31-48.~~ [Liu, X., Zhang, Y., and Zhang, D.: Permeability characteristics of fractured](#)
1258 [granite under varying stress conditions, Rock Mechanics and Rock Engineering, 54\(3\),](#)
1259 [937–952, 2021.](#)

1260 [49.](#) [Majumdar, R.K., and Das, D.: Hydrological characterization and estimation of aquifer](#)
1261 [properties from electrical sounding data in Sagar Island region, South 24 Parganas, West](#)
1262 [Bengal, India, Asian J Earth Sci, 4, 60–74, 2011.](#)

1263 [50.](#) [Margat, J., and van der Gun, J.: Groundwater around the world: A geographic synopsis.](#)
1264 [CRC Press, 2013. <https://doi.org/10.1201/b13977>.](#)

1265 [51.](#) [McKeown, C., Haszeldine, R.S., and Couples, G.D.: Mathematical modelling of](#)
1266 [groundwater flow at Sellafield, UK. Engineering Geology, 52\(3–4\), 231–250, 1999.](#)

1267 ~~32-52.~~ [Medici, G., Ling, F., and Shang, J.: Review of discrete fracture network](#)
1268 [characterization for geothermal energy extraction, Frontiers in Earth Science, 11,](#)
1269 [1328397, 2023.](#)

1270 53. Mira Geoscience Ltd.: GOCAD Mining Suite 3D Geological Modeling Software. Nancy
1271 University, Lorraine, France, 1999.

1272 33-54. MOHURD (Ministry of Housing and Urban-Rural Development of the People's
1273 Republic of China): National Groundwater Resources Strategic Survey and Planning
1274 Guidelines (in Chinese). Beijing: China Geological Press, 2021.

1275 55. Mudunuru, M.K., Cromwell, E.L.D., Wang, H., and Chen, X.: Deep learning to estimate
1276 permeability using geophysical data, *Advances in Water Resources*, 167, 104272, 2022.

1277 56. Neuzil, C.E.: How permeable are clays and shales? *Water Resources Research*, 30(2),
1278 145–150, 1994.

1279 34-57. Niu, G., Chen, M., and Fan, L.: Stress-dependent permeability of fractured granite
1280 and its implications for enhanced geothermal systems, *Geothermics*, 64, 294–303, 2016.

1281 35-58. Niwas, S., and De Lima, O.A.L.: Aquifer parameter estimation from surface
1282 resistivity data, *Groundwater*, 41, 94–99, 2003.

1283 59. Nwosu, L.I., Nwankwo, C.N., and Ekine, A.S.: Geoelectric investigation of the hydraulic
1284 properties of the aquiferous zones for evaluation of groundwater potentials in the
1285 complex geological area of imostate, Nigeria, *Asian J Earth Sci*, 6, 1–15, 2013.

1286 36-60. Paterson, M.S., and Wong, T.F.: *Experimental Rock Deformation: The Brittle*
1287 Field, Springer, 2005.

1288 37-61. Pellet, H., Arfib, B., Henry, P., Tournon, S., and Gassier, G.: Mesoscale
1289 permeability variations estimated from natural airflows in the decorated Cosquer Cave
1290 (southeastern France), *Hydrol. Earth Syst. Sci.*, 28, 4035–4057, 2024.

1291 38-62. Phoenix Geophysics CMTPro, The Canadian Phoenix CMT Pro Version software
1292 for CSAMT data processing. Toronto, Ontario, Canada, 2020.

Formatted: Font: (Asian) +Body Asian,
Pattern: Clear (White)

Formatted: Font: (Asian) +Body Asian,
Pattern: Clear (White)

Formatted: Font: (Default) Times New
Roman, 12 pt

1293 ~~39-63.~~ Phoenix Geophysics CSAMT-SW, The Canadian Phoenix CSAMT-SW Version
1294 software for CSAMT data inversion. Toronto, Ontario, Canada, 2020.

1295 ~~40-64.~~ Qian, H., Wang, Y., Zhang, Y., and Su, Y.: Advances in deep groundwater
1296 exploration and management under climatic stress in arid regions of China, Journal of
1297 Hydrology, 626, 130234, 2024.

1298 ~~41-65.~~ Qin, X.: Application of Unwedge program to geological stability analysis of deep
1299 buried deposits, Comprehensive, 8, 270–273, 2017 (In Chinese)

1300 ~~66.~~ Refsgaard, J.C., Arbjerg-Nielsen, K., Drews, M., Halsnæs, K., Jeppesen, E., Madsen, H.,
1301 and Christensen, J.H.: The role of uncertainty in climate change adaptation strategies – A
1302 Danish water management example, Mitigation and Adaptation Strategies for Global
1303 Change, 18(3), 337–359, 2012.

1304 ~~67.~~ Revil, A., and Cathles, L.M.: Permeability of shaly sands, Water Resources Research,
1305 35(3), 651–662, 1999.

1306 ~~42-68.~~ Roa-García, M.C., Brown, S., Schreier, H., and Lavkulich, L.M.: The role of land
1307 use and soils in regulating water flow in small headwater catchments of the Andes, Water
1308 Resources Research, 47(5), 2010.

1309 ~~43-69.~~ Robinson, J., Slater, L., Johnson, T., Shapiro, A., Tiedeman, C., Ntarlagiannis, D.,
1310 Johnson, C., Day-Lewis, F., Lacombe, P., Imbrigiotta, T., and Lane, J.: Imaging
1311 pathways in fractured rock using three-dimensional electrical resistivity tomography,
1312 Groundwater, 54 (2), 186–201, 2016.

1313 ~~44-70.~~ Rodell, M., Velicogna, I., and Famiglietti, J.S.: Satellite-based estimates of
1314 groundwater depletion in India, Nature, 460 (7258), 999–1002, 2009.

Formatted: Font: (Asian) +Body Asian

Formatted: Font: (Default) Times New Roman, 12 pt

1315 | ~~45-71.~~ Rodi, W., and Mackie, R.L.: Nonlinear conjugate gradients algorithm for 2-D
1316 | magnetotelluric inversion, *Geophysics*, 66 (1), 174–187, 2001.

1317 | ~~46-72.~~ Simpson, F., and Bahr, K.: *Practical magnetotellurics*. Cambridge University
1318 | Press, Cambridge. 254 pp, 2005.

1319 | 73. Singh, K.P.: Nonlinear estimation of aquifer parameters from surficial resistivity
1320 | measurements, *Hydrology and Earth System Sciences Discussions*, 2 (3), 917–938, 2005.

1321 | ~~47-74.~~ Singh, R., Prasad, M., and Al-Tahini, A.: A comparative study of electrical and
1322 | hydraulic properties in carbonate and siliciclastic rocks, *Geophysical Journal*
1323 | *International*, 221(3), 1837–1855, 2020.

1324 | ~~48-75.~~ Sinha, R., Israil, M., and Singhal, D.C.: A hydrogeological model of the
1325 | relationship between geoelectric and hydraulic parameters of anisotropic aquifers,
1326 | *Hydrogeol J*, 17, 495–503, 2009.

1327 | ~~49-76.~~ Smith, J.T., and Booker, J.R.: Rapid inversion of two-and three-dimensional
1328 | magnetotelluric data, *Journal of Geophysical Research: Solid Earth*, 96 (B3), 3905–3922,
1329 | 1991.

1330 | ~~50-77.~~ Soupios, P.M., Kouli, M., Vallianatos, F., Vafidis, A., and Stavroulakis, G.:
1331 | Estimation of aquifer hydraulic parameters from surficial geophysical methods: a case
1332 | study of Keritis Basin in Chania (Crete–Greece), *J Hydrol*, 1, 122–131, 2007.

1333 | ~~51-78.~~ Vouillamoz, J.M., Lawson, F.M.A., Yalo, N., and Descloitres, M.: The use of
1334 | magnetic resonance sounding for quantifying specific yield and transmissivity in hard
1335 | rock aquifers: the example of Beni, *J Appl Geophys*, 107, 16–24, 2014.

Formatted: Pattern: Clear

Formatted: Font: (Default) Times New Roman, 12 pt

1336 ~~52-79.~~ Wada, Y., Van Beek, L.P., Van Kempen, C.M., Reckman, J.W., Vasak, S., and
1337 Bierkens, M.F.: Global depletion of groundwater resources, *Geophysical Research*
1338 *Letters*, 37 (20), 2010.

1339 80. Wang, R., Yin, C., Wang, M., and Di, Q.: Laterally constrained inversion for CSAMT
1340 data interpretation, *Journal of Applied Geophysics*, 121, 63–70, 2015.

1341 81. Wang, W., Xie, X., Zhang, Y., Yang, J., and Liu, C.: Hydrogeological properties of
1342 fractured sandstones in southern China, *Hydrogeology Journal*, 22(5), 1127–1142, 2014.

1343 ~~53-82.~~ Waxman, M.H., and Smits, L.J.M.: Electrical conductivities in oil-bearing shaly
1344 sands, *Society of Petroleum Engineers Journal*, 8(02), 107–122, 1968.

1345 ~~54-83.~~ Webring, M.W.: MINC: A Gridding Program Based on Minimum Curvature: U.S.
1346 Geological Survey Open File Report, 81–1224, p. 41p, 1981.

1347 ~~55-84.~~ Worthington, S.R.H., Davies, G.J., and Alexander, E.C. Jr.: Enhancement of
1348 bedrock permeability by weathering, *Earth-Sci Rev*, 160, 188–202, 2016.

1349 ~~56-85.~~ Wynn, J., Mosbrucker, A., Pierce, H., and Spicer, K.: Where is the hot rock and
1350 where is the ground water-using CSAMT to map beneath and around Mount St. Helens,
1351 *Journal of Environmental and Engineering Geophysics*, 21, 79–87, 2016.

1352 ~~57-86.~~ Yadav, G.S., and Singh, S.K.: Integrated resistivity surveys for delineation of
1353 fractures for ground water exploration in hard rock areas, *Journal of Applied*
1354 *Geophysics*, 62 (3), 301–312, 2007.

1355 ~~58-87.~~ Yan, Y., Ma, L., Qian, J., Zhao, G., Fang, Y., Ma, H., and Wang, J.: Estimating
1356 permeability of rock fracture based on geometrical aperture using geoelectrical
1357 monitoring, *Journal of Hydrology*, 644, 132067, 2024.

Formatted: Border: : (No border), Pattern: Clear

Formatted: Border: : (No border), Pattern: Clear

Formatted: Font: (Default) Times New Roman, 12 pt

1358 | ~~59-88.~~ Yang, H.Q., and Zhang, L.: Bayesian back analysis of unsaturated hydraulic
1359 | parameters for rainfall-induced slope failure: A review, *Earth-Science Reviews*, 251,
1360 | 104714, 2024.

1361 | ~~60-89.~~ Yang, J., Zhang, H., and Cui, Z.: Stability Analysis and Countermeasures of Rock
1362 | Block in Underground Cavern, *Guangdong Water Resources and Hydropower* 5, 23–27,
1363 | 2021 (In Chinese)

1364 | ~~61-90.~~ Zhang, F., Zhou, Z., Huang, Y., and Chen, Z.: Determining the Permeability of
1365 | Fractured Rocks Based on Joint Mapping, *Groundwater*, 42, 509–515, 2004.

1366 | 91. Zhang, J., Sirieix, C., Genty, D., Salmon, F., Verdet, C., Mateo, S., Xu, S., Bujan, S.,
1367 | Devaux, L., and Larcanché, M.: Imaging hydrological dynamics in karst unsaturated
1368 | zones by time-lapse electrical resistivity tomography, *Science of the Total Environment*
1369 | 907, 168037, 2024.

1370 | ~~62-92.~~ Zhang, L., Yang, C., and Qin, S.: Evaluation of groundwater flow in granite using
1371 | core-based permeability and fracture analysis, *Journal of Hydrology*, 585, 124775, 2020.

1372 | 93. Zhang, M., Farquharson, C.G., and Li, C.: Improved controlled source audio-frequency
1373 | magnetotelluric method apparent resistivity pseudo-sections based on the frequency and
1374 | frequency–spatial gradients of electromagnetic fields, *Geophysical Prospecting*, 69, 474–
1375 | 490, 2021.

1376 | ~~63-94.~~ Zhao, Y., Xu, T., and Luo, G.: Statistical analysis of rock permeability variation
1377 | in different lithologies, *Engineering Geology*, 239, 123–133, 2018.

1378 | ~~64-95.~~ Zhu, L., Gong, H., Dai, Z., Guo, G., and Teatini, P.: Modeling 3-D permeability
1379 | distribution in alluvial fans using facies architecture and geophysical acquisitions, *Hydrol.*
1380 | *Earth Syst. Sci.*, 21, 721–733, 2017.

1381 | ~~65-96.~~ Zonge, K.L., and Hughes, L.J.: Electromagnetic Methods—Theory and Practice,
1382 | 1988.